

# Modeling Athermal Phonons in Novel Materials using the G4CMP Simulation Toolkit

I. Hernandez<sup>a,b,\*</sup>, R. Linehan<sup>b,\*</sup>, R. Khatiwada<sup>a,b</sup>, E. Figueroa-Feliciano<sup>d,b</sup>, L. Hsu<sup>b</sup>, K. Anyang<sup>a,b</sup>, G. Bratrud<sup>b,d</sup>, D. Temples<sup>b</sup>, D. Baxter<sup>b,d</sup>, M. Kelsey<sup>c</sup>

<sup>a</sup>*Illinois Institute of Technology, Department of Physics, Chicago, IL 60616, USA*

<sup>b</sup>*Fermi National Accelerator Laboratory, Batavia, IL 60510, USA*

<sup>c</sup>*Texas A&M University, 400 Bizzell St. College Station, TX 77843*

<sup>d</sup>*Department of Physics & Astronomy, Northwestern University, Evanston, IL 60208, USA*

## Abstract

Understanding phonon and charge propagation in superconducting devices plays an important role in both performing low-threshold dark matter searches and limiting correlated errors in superconducting qubits. The Geant4 Condensed Matter Physics (G4CMP) package, originally developed for the Cryogenic Dark Matter Search (CDMS) experiment, models charge and phonon transport within silicon and germanium detectors and has been validated by experimental measurements of phonon caustics, mean charge-carrier drift velocities, and heat pulse propagation times. In this work, we present a concise framework for expanding the capabilities for phonon transport to a number of other novel substrate materials of interest to the dark matter and quantum computing communities, including sapphire ( $\text{Al}_2\text{O}_3$ ), Gallium Arsenide (GaAs), Lithium Fluoride (LiF), Calcium Tungstate ( $\text{CaWO}_4$ ), and Calcium Fluoride ( $\text{CaF}_2$ ). We demonstrate the use of this toolkit in generating phonon transport properties of these materials and compare these properties with experimentally-determined values where available.

*Keywords:* Phonon, Simulation, G4CMP, Dark Matter, Material Science, Qubits, Sapphire

## 1 Introduction

Mounting astrophysical and cosmological observations indicate the existence and abundance of a cold, frictionless nonbaryonic “dark” matter in the universe [1, 2, 3]. As direct detection searches for particle-like candidates with masses above the  $\text{GeV}/c^2$  scale have yielded only null results in the past few decades [4, 5], there has recently been increased interest in developing low-energy threshold detectors capable of probing parameter space at lower masses, down to the  $\text{keV}/c^2$  scale [6]. A common class of such detectors rely on cryogenic (mK) solid-state substrates coupled to superconducting films, in which energy depositions in the substrate generate phonon excitations that can be sensed in the films [7, 8, 9, 10]. These phonons may be generated from a number of different potential interaction types: direct nuclear recoils of dark matter on lattice ions, phonons produced from electron-hole recombination after a dark matter ionization event, and Neganov-Trofimov Luke phonons from drifting freed electrons through the crystal using an electrostatic field. The phonon response of sil-

icon and germanium under these effects has been well-studied [11, 12, 13, 14]

In recent years there has been a broadening of the landscape of materials proposed for phonon-mediated cryogenic dark matter search experiments. While historically these detectors have been made from silicon, germanium, calcium tungstate ( $\text{CaWO}_4$ ), or calcium fluoride ( $\text{CaF}_2$ ) [15, 16, 17, 18], future dark matter detectors may benefit from other carefully chosen novel target materials. For example, polar crystals like sapphire ( $\text{Al}_2\text{O}_3$ ) and gallium arsenide (GaAs) increase sensitivity to DM candidates coupling to the dark photon. These materials, especially those with many accessible optical modes, give sufficiently strong directional dependence of DM scattering rates to enable daily modulation searches, increasing DM discovery power [19, 20]. A thorough grasp of (and ability to model) phonon propagation in these materials will be required for signal- and background-model building in these experiments.

Moreover, some of these materials (like sapphire) are commonly used in the quantum computing community as chip substrates due to their low dielectric losses [21]. As superconducting qubits have been shown to experience catastrophic correlated errors due to the presence of phonons pro-

\*Corresponding authors: ihernandez6@hawk.iit.edu and linehan3@fnal.gov

52 duced by ionizing radiation, quantitatively under-  
53 standing phonon transport in such chips may facil-  
54 itate developing strategies that mitigate such er-  
55 rors [22, 23, 24, 25].

56 Modeling phonon propagation in novel mate-  
57 rials is therefore a foundation for studying sig-  
58 nals and backgrounds in particle-like dark matter  
59 searches and sources of correlated errors in super-  
60 conducting qubits. The Geant4 Condensed Mat-  
61 ter Physics (G4CMP) package is an open-source  
62 particle-tracking simulation tool built to perform  
63 this modeling, originally in the context of low-mass  
64 dark matter experiments [26]. While it success-  
65 fully models phonon transport within silicon and  
66 germanium substrates, it currently does not in-  
67 clude information for phonon propagation in other  
68 target materials. As other substrate materials are  
69 adopted in dark matter searches or quantum com-  
70 puting, a thorough understanding of chip response  
71 to energy depositions will rely on a corresponding  
72 expansion of the set of materials in which G4CMP  
73 can model phonon transport.

74 In this work we achieve an expansion of  
75 G4CMP’s phonon-modeling capability for a large  
76 number of materials of interest to the low-mass  
77 dark matter and quantum information communi-  
78 ties, and provide a framework for extending this  
79 to further materials. In Section 2, we discuss the  
80 phonon physics that underlies G4CMP’s transport  
81 modeling and present the set of parameters needed  
82 for modeling phonon response in a new material.  
83 In Section 3, we calculate this set of parameters  
84 for several new materials, demonstrate successful  
85 integration into G4CMP, and validate the results  
86 against experimental results available in the lit-  
87 erature. We discuss potential extensions to this  
88 modeling and its impact on dark matter detection  
89 and quantum computing efforts in Section 4, and  
90 conclude in Section 5.

## 91 2 Phonon Kinematics

92 When high-energy phonons are created from  
93 energy deposits in a chip, the system evolves in  
94 a way governed by several distinct phonon kine-  
95 matics processes. We consider as an example an  
96 optical phonon created from a DM scatter in the  
97 substrate. First, this phonon can undergo anhar-  
98 monic decay into multiple lower-energy phonons  
99 via one of several possible channels, including  
100 the Klemens channel<sup>1</sup> ( $\text{LO} \rightarrow \text{XA} + \text{XA}$ ), the Ri-

dley Channel ( $\text{LO} \rightarrow \text{TO} + \text{XA}$ ), and the Valée-  
101 Bogani channel ( $\text{LO} \rightarrow \text{LO} + \text{XA}$ ) [27]. All of these  
102 optical phonon decay channels occur on  $\mathcal{O}(ps)$   
103 timescales. Once downconversion from the optical  
104 branch phonons to acoustic branch phonons oc-  
105 curs, there is further downconversion of the acous-  
106 tic phonons, fragmenting the initial phonon energy  
107 even more. Scattering on isotopic impurities may  
108 change acoustic phonon’s trajectories and polar-  
109 izations, and has been noted to possibly also play  
110 a role in phonon thermalization [28]. Selection of  
111 the proper final-state phonon polarizations during  
112 downconversion and scattering is governed by the  
113 fractional density of states (DOS) for the various  
114 possible phonon polarizations. At sufficiently low  
115 acoustic phonon energies, the scattering and down-  
116 conversion mean free paths may extend beyond the  
117 substrate dimensions, and the phonon trajectory  
118 becomes limited by boundary scatters (i.e. enters  
119 the “ballistic regime”). At all energies, phonon  
120 propagation is governed by the substrate’s crystal  
121 structure, leading to formation of caustics, pre-  
122 ferred directions into which phonons’ group veloci-  
123 ties are focused by the crystal anisotropy. G4CMP  
124 simulates the subset of these physical processes  
125 involving acoustic phonons: acoustic phonon an-  
126 harmonic downconversion, isotopic scattering, and  
127 transport along caustics.<sup>2</sup>

128 The set of parameters needed to integrate this  
129 physics into G4CMP for a given material is enu-  
130 merated in Table 1. Because rigorous model-  
131 ing of some of the above-mentioned physics pro-  
132 cesses in a fully anisotropic medium is nontriv-  
133 ial, it is often useful to simplify calculations using  
134 the “isotropic continuum approximation,” (ICA)  
135 in which phonons are assumed to be long enough in  
136 wavelength that anisotropy in the crystal may be  
137 ignored [29]. While we (and G4CMP) use this ap-  
138 proximation to simplify calculations of the rate co-  
139 efficients for anharmonic decay and isotopic scat-  
140 tering, the DOS and caustics modeling fully ac-  
141 counts for the anisotropic crystal structure.

142 The thrust of this section is to discuss the  
143 mathematical foundation for these physics pro-  
144 cesses and estimate the corresponding required  
145 simulation parameters for a set of substrates useful  
146 to the dark matter detection community. In doing  
147 so we also hope to provide a streamlined recipe  
148 for performing this G4CMP upgrade for any other  
149 materials later deemed of interest to the cryogenic  
150 instrumentation community.

151 <sup>2</sup>While scattering and downconversion of phonons at  
152 surfaces is simulated in G4CMP, the complexity of that  
153 topic puts it beyond the scope of this work. Optical  
154 phonons are not simulated in G4CMP.

<sup>1</sup>Here, LO indicates longitudinal optical phonon modes,  
TO indicates transverse optical modes, and XA indicates  
either longitudinal or transverse acoustic modes. In the  
acoustic mode, we keep this general as arbitrary combina-  
tions may be energetically prohibited in certain materials  
depending on the phonon dispersion.

Table 1: Parameters required for G4CMP to model phonon transport within a given solid-state material.

Parameter	Units	Description
$C_{ij}$	GPa	Second-order elastic constants
$\mu$	GPa	Lamé constant, 2nd-order isotropic elastic constant
$\lambda$	GPa	Lamé constant, 2nd-order isotropic elastic constant
$\beta$	GPa	3rd-order isotropic elastic constant
$\gamma$	GPa	3rd-order isotropic elastic constant
$A$	s <sup>4</sup>	Anharmonic downconversion rate coefficient
$B$	s <sup>3</sup>	Isotropic scattering rate coefficient
$F_{TT}$	None	Fraction of $L \rightarrow TT$ downconversion
LDOS	None	Longitudinal phonons' density of states (fractional)
STDOS	None	Slow transverse phonons' density of states (fractional)
FTDOS	None	Fast transverse phonons' density of states (fractional)
Debye Energy	THz	Debye Energy for phonon primaries

## 2.1 Anharmonic Downconversion

Anharmonic decay of an acoustic phonon into two lower-energy acoustic phonons is phonon-polarization-dependent. Under the isotropic continuum approximation, this decay can only proceed for initial longitudinally-polarized phonons, and can only proceed via two potential decay channels:  $L \rightarrow L + T$  and  $L \rightarrow T + T$ , in which the final products are a longitudinal (L) and transverse (T) phonon and two transverse phonons, respectively. Here, transverse phonons can be either on the transverse-slow phonon branch or transverse-fast phonon branch. Though beyond the scope of this work's modeling, we also note for completeness that additional decay modes, including those for transverse phonons, are possible if the ICA is relaxed [30, 31, 32].

Formally, the combined  $L \rightarrow T + T$  and  $L \rightarrow L + T$  rate of anharmonic decay within a crystal can be calculated by adding the third-order terms of the crystal's potential energy to the Hamiltonian governing the crystal's evolution. Using first-order time-dependent perturbation theory, one can derive a characteristic mode decay rate,  $\Gamma_{\text{anharmonic}}$ , with the following form:

$$\Gamma_{\text{anharmonic}} = A\nu^5, \quad (1)$$

where  $A$  is a temperature-independent constant [29, 33] and  $\nu$  is the phonon frequency. This form holds for normal (i.e. non-Umklapp) phonon processes at low temperatures ( $k_B T \ll h\nu$ ).

Calculating the constant  $A$  in Equation 1 relies on knowing the second- and third-order elastic constants considered in the total potential energy of the material. Here, it is useful to apply the ICA, giving rise to a separate set of “isotropic elastic constants:” the Lamé constants  $\mu$  and  $\lambda$  at second order, and a set of three constants  $\alpha$ ,  $\beta$ , and  $\gamma$  at third order. Ref. [33] gives the  $L \rightarrow T + T$  and

$L \rightarrow L + T$  decay rates in terms of these parameters.

To numerically calculate the phonon anharmonic decay rate in a material of a specific crystal structure, the isotropic elastic constants  $\mu$ ,  $\lambda$ ,  $\alpha$ ,  $\beta$ , and  $\gamma$  can be expressed using the *true* second-order elastic constants  $C_{ijkl}$  and third-order elastic constants  $C_{ijklmn}$  corresponding to the material's crystal group. A general form of this parameterization is found using the development by Ref. [34], where Einstein notation is used:

$$\mu = (3C_{lkk} - C_{llk})/30$$

$$\lambda = (2C_{lkk} - C_{llk})/15$$

$$\alpha = (8C_{iillnn} - 15C_{iilnln} + 8C_{inilln}) / 105 \quad (2)$$

$$\beta = (-5C_{iillnn} + 19C_{iilnln} - 12C_{inilln}) / 210$$

$$\gamma = (2C_{iillnn} - 9C_{iilnln} + 9C_{inilln}) / 210.$$

For a specific crystal space group these parameters can be calculated by taking advantage of symmetries present in the second- and third-order elastic constants [35]. Most of the materials of interest to the dark matter search community that we consider here, including Si, Ge, GaAs, LiF and CaF<sub>2</sub>, belong to cubic space groups. For these, space-group-specific expressions for the second- and third-order isotropic elastic constants have been documented extensively in literature, and as a result we do not reproduce them here [34, 33, 36]. However, a few materials of interest, including sapphire (Al<sub>2</sub>O<sub>3</sub>) and calcium tungstate (CaWO<sub>4</sub>), have non-cubic space groups for which expressions of  $\alpha$ ,  $\beta$ ,  $\gamma$ ,  $\mu$ , and  $\lambda$  have not yet been documented in literature (to the authors' knowledge). In Table 2, we present expressions for these in terms of the materials' third-order elastic constants, using Voigt notation [37] for reduction from  $2n$  to  $n$  in-

Table 2: Expressions for the Lamé constants and third-order isotropic elastic coefficients, calculated for the two non-cubic space groups (for which such expressions could not be found in literature). The space groups for these two materials are included for completeness.

Material	Space Group	Parameter	Expression
Al <sub>2</sub> O <sub>3</sub>	R̄3c	$\mu$	$(2C_{11} - C_{12} - 2C_{13} + C_{33} + 6C_{44} + 3C_{66})/15$
		$\lambda$	$(2C_{11} + 4C_{12} + 8C_{13} - 4C_{44} + C_{33} - 2C_{66})/15$
		$\alpha$	$(-17C_{111} + 30C_{112} + 33C_{113} + 78C_{123} - 57C_{133} - 156C_{144} + 84C_{155} - 17C_{222} + C_{333} - 12C_{344})/105$
		$\beta$	$(71C_{111} + 4C_{112} - 11C_{113} - 68C_{123} + 103C_{133} + 220C_{144} - 140C_{155} - 55C_{222} + 2C_{333} + 4C_{344})/210$
		$\gamma$	$(-34C_{111} - 24C_{112} + 3C_{113} + 30C_{123} - 51C_{133} - 144C_{144} + 126C_{155} + 92C_{222} + 2C_{333} + 18C_{344})/210$
		$\mu$	$(2C_{11} - C_{12} - 2C_{13} + C_{33} + 6C_{44} + 3C_{66})/15$
CaWO <sub>4</sub>	I4 <sub>1</sub> /a	$\lambda$	$(2C_{11} + 4C_{12} + 8C_{13} + C_{33} - 4C_{44} - 2C_{66})/15$
		$\alpha$	$(2C_{111} + 18C_{112} + 42C_{113} + 48C_{123} - 6C_{133} - 60C_{144} - 12C_{155} - 12C_{166} + C_{333} - 12C_{344} - 30C_{366} + 12C_{456})/105$
		$\beta$	$(4C_{111} + 8C_{112} - 7C_{113} - 30C_{123} + 23C_{133} + 76C_{144} + 4C_{155} + 4C_{166} + 2C_{333} + 4C_{344} + 38C_{366} - 72C_{456})/210$
		$\gamma$	$(2C_{111} - 3C_{112} + 6C_{123} - 6C_{133} - 18C_{144} + 9C_{155} + 9C_{166} + C_{333} + 9C_{344} - 9C_{366} + 27C_{456})/105$

dices, where  $n$  is the order of the elastic constant.

Once these isotropic second- and third-order elastic constants are calculated for a material, the value  $A$  in Equation 1 can be calculated via the treatment in Ref. [33], and used as an input to G4CMP. Results of our calculations for various materials of interest are presented in Section 3.1.

## 2.2 Isotopic Scattering

Phonons may also be scattered on isotopic impurities in the crystal, where slight variations in atomic mass break the regularity in the crystal structure. Considering these impurities as a small perturbation to the otherwise uniform crystal Hamiltonian, one can again use perturbation theory to obtain an expression for the scattering rate of a single phonon via this channel [29]. This rate is proportional to the fourth power of phonon energy:

$$\Gamma_{\text{isotopic}} = B\nu^4 \quad (3)$$

$$= \frac{4\pi^3 \Gamma_{md} \Omega}{\langle c^3 \rangle} \nu^4, \quad (4)$$

where  $\Omega$  is the volume per atom in the crystal unit cell,  $\langle c^3 \rangle$  is the polarization-averaged (cubed) speed of sound in the material, and  $\Gamma_{md}$  is a mass defect coefficient capturing the average deviation of the crystal from isotopic purity [38, 39]. This expression holds true in the isotropic continuum approximation, which holds for phonons with long wavelengths relative to the interatomic spacing.

The mass defect coefficient is given by [40, 41]

$$\Gamma_{md} = \frac{\langle \overline{\Delta M^2} \rangle}{\langle \overline{M} \rangle^2}, \quad (5)$$

where  $\langle \overline{\Delta M^2} \rangle$  refers to the average mass variance and  $\langle \overline{M} \rangle^2$  is the average mass. The average mass of each component is given by the stoichiometry-weighted average of each site average mass  $\overline{M}_n$

$$\langle \overline{M} \rangle = \frac{\sum_n c_n \overline{M}_n}{\sum_n c_n} \quad (6)$$

$$\overline{M}_n = \sum_i f_{i,n} M_{i,n}. \quad (7)$$

where the index  $n$  refers to the the  $n^{th}$  atom of the chemical formula, the index  $i$  refers to isotope  $i$  of atom  $n$ ,  $M_{i,n}$  refers to the atomic mass of the  $i^{th}$  isotope of atom  $n$ ,  $\overline{M}_n$  is the average isotopic mass of atom  $n$ , and  $f_i(n)$  refers to the fractional abundance of the  $i^{th}$  isotope of atom  $n$ .<sup>3</sup> In the same way, the average mass variance is

$$\langle \overline{\Delta M^2} \rangle = \frac{\sum_n c_n \overline{\Delta M_n^2}}{\sum_n c_n} \quad (8)$$

$$\overline{\Delta M_n^2} = \sum_i f_{i,n} (M_{i,n} - \overline{M}_n)^2. \quad (9)$$

<sup>3</sup>We note here that formally, the sum over  $i$  may be different for different atoms  $s$  in the unit cell.

257 In this development, our use of the isotropic con-  
 258 tinuum approximation implies that Equation 3  
 259 represents an average scattering rate for all acous-  
 260 tic phonon polarizations. While we use this defi-  
 261 nition in this work, it is worth noting that other  
 262 interpretations of the mass defect coefficient have  
 263 also been used [42, 43].

264 Once the coefficient  $B$  is calculated, it can be  
 265 input into G4CMP to model isotopic scattering,  
 266 where it acts as the scattering rate coefficient for  
 267 all three phonon polarizations. We present the re-  
 268 sults of this calculation of  $B$  for several materials  
 269 of interest in Section 3.2.

### 270 2.3 Density of States (DOS)

271 During both anharmonic downconversion pro-  
 272 cesses and isotopic scattering processes (discussed  
 273 in Section 2.2) G4CMP uses the phonon density of  
 274 states to determine the randomly-drawn polariza-  
 275 tions of phonons produced after downconversions  
 276 and scatters. The LDOS, STDOS, and FTDOS  
 277 parameters in Table 5 are the fractional densities  
 278 of states for longitudinal, slow transverse, and fast  
 279 transverse acoustic phonons, respectively, and sum  
 280 to unity.

281 The calculation of the DOS values for these  
 282 materials is performed in two steps: computation  
 283 of a 3D phonon dispersion relationship  $\omega(\vec{k})$  for  
 284 a material using its lattice properties, and com-  
 285 putation of the DOS from the phonon disper-  
 286 sion relationship. For each material, we use lat-  
 287 tice force constant information from the Materials  
 288 Data Repository [44] as an input to Phonopy, a  
 289 separate software used in the calculation of three-  
 290 dimensional phonon dispersion relationships [45,  
 291 46].<sup>4</sup> From these dispersion curves, which are cal-  
 292 culated at a discrete grid of  $\omega(\vec{k})$  points for each  
 293 branch, we compute the contribution of the DOS  
 294 per phonon branch  $\lambda$  at given frequency  $\omega$ , defined  
 295 as

$$g_\lambda(\omega) = \frac{1}{N} \sum_i \delta(\omega - \omega_i). \quad (10)$$

296 Here, the sum is over all phonon frequencies  $\omega_i$  of  
 297 this branch in the first Brillouin zone, and  $N$  is  
 298 the total number of grid points in the first Bril-  
 299 louin zone. In practice, the delta function in this  
 300 expression is treated as a gaussian of finite width.  
 301 From this expression, we can obtain the fractional  
 302 contribution at 1 THz for acoustic phonons, which  
 303 is the fractional DOS input required by G4CMP.  
 304 Moreover, calculating the total DOS we can obtain  
 305 the maximum acoustic phonon energy and maxi-  
 306 mum optical phonon energy (Debye Energy), the  
 307 latter of which is also an input to G4CMP.

### 298 2.4 Propagation along Caustics

308 The propagation of acoustic phonons in a crys-  
 309 tal is governed by the Green-Christoffel equation:  
 310

$$\rho\omega^2\epsilon_i = C_{ijkl}k_jk_k\epsilon_l, \quad (11)$$

311 where  $\omega$  is the phonon frequency,  $\epsilon_\mu$  is the  
 312 phonon polarization (longitudinal, transverse fast  
 313 and transverse slow),  $k$  is the phonon wavevec-  
 314 tor,  $\rho$  is the crystal's mass density, and  $C_{ijkl}$  is  
 315 again the elastic constant tensor. This equation  
 316 arises from considering plane monochromatic elas-  
 317 tic wave solutions to the equations governing an  
 318 elastically deformed medium.

319 Propagation direction is governed by the group  
 320 velocity  $\vec{v}_g = \vec{\nabla}_{\vec{k}}\omega$ . As a result of an arbitrary  
 321 crystal's anisotropic elastic tensor  $C_{ijkl}$ , the group  
 322 velocity of a phonon may not be parallel with  
 323 the phonon's wavevector  $\vec{k}$  [48, 49]. An initially  
 324 isotropic distribution of wavevector  $\vec{k}$  therefore in  
 325 general gives a nonuniform distribution of group  
 326 velocity. This leads to a phenomenon known as  
 327 "phonon focusing" in a crystal, from which "caus-  
 328 tic" patterns are formed (Figure 3). These have  
 329 been measured experimentally in several experi-  
 330 mental setups for a variety of different materials  
 331 [50, 51, 52].

332 To successfully characterize acoustic phonon  
 333 propagation direction in a new material, one then  
 334 only requires the second-order elastic tensor com-  
 335 ponents  $C_{ijkl}$  for the new material. These elas-  
 336 tic tensor components used in this work are avail-  
 337 able for Al<sub>2</sub>O<sub>3</sub> [53], GaAs [54], CaWO<sub>4</sub> [55],  
 338 CaF<sub>2</sub> [31], and LiF [56]. For simulating phonon  
 339 propagation in a new material, G4CMP only re-  
 340quires these second-order elastic tensor compo-  
 341 nents. While in practice the caustic patterns  
 342 emerging from crystal anisotropies are dependent  
 343 on the energy of the phonon [54], G4CMP does not  
 344 yet include this energy dependence and instead ap-  
 345 proximates this dependence as being weak in the  
 346 limit of low phonon energy.

## 3 Model Results and Validation

347 In this section we demonstrate the above cal-  
 348 culations as applied to Si, Ge, GaAs, Al<sub>2</sub>O<sub>3</sub>, LiF,  
 349 CaWO<sub>4</sub>, and CaF<sub>2</sub>, and where possible use exist-  
 350 ing literature measurements to do a coarse vali-  
 351 dation of our calculations and the implementation  
 352 into G4CMP. These are done for all four physi-  
 353 cal properties discussed in the subsections of Sec-  
 354 tion 2: anharmonic downconversion, isotopic scat-  
 355 tering, phonon density of states (DOS) and prop-  
 356 agation along caustics.

<sup>4</sup>Materials files used for CaWO<sub>4</sub> were from Ref. [47].

Table 3: Anharmonic downconversion parameters for a variety of target materials of interest. The calculated Lamé parameters ( $\mu$ ,  $\lambda$ ) and third-order isotropic elastic coefficients ( $\alpha$ ,  $\beta$ ,  $\gamma$ ) (units of pressure) are used to compute the anharmonic decay rate coefficient  $A$  found in Equation 1 and are included for completeness. For comparison, we include calculated literature values  $A_{c,l}$  and measured literature values  $A_{m,l}$  for these materials where available. Values of  $A_{c,l}$  do not always assume the same isotropic continuum approximation used in our calculation of  $A$ , and may quote a range of rates representing multiple propagation directions.  $A_{m,l}$  was difficult to find in the literature for most materials here. We were also unable to find literature values for the third-order elastic constants of CaWO<sub>4</sub> for calculation of  $\alpha$ ,  $\beta$ , and  $\gamma$ , but nonetheless include CaWO<sub>4</sub> as other literature calculations of  $A_{c,l}$  were found. For literature values  $A_{c,l}$  and  $A_{m,l}$ , references are provided after the stated values.

Material	$\mu$ [GPa]	$\lambda$ [GPa]	$\alpha$ [GPa]	$\beta$ [GPa]	$\gamma$ [GPa]	$F_{TT}$	$A$ [ $10^{-55} \text{ s}^4$ ]	$A_{c,l}$ [ $10^{-55} \text{ s}^4$ ]	$A_{m,l}$ [ $10^{-55} \text{ s}^4$ ]
Si	68.58	53.68	-227.37	-55.97	-107.97	0.75	1.15	0.741 [33]	—
Ge	56.6	33.6	-179.3	-60.5	-82.1	0.72	6.8	16.5 [33]	—
GaAs	44.2	47.2	-170.11	-54.71	-67.51	0.77	7.77	7.7–13.5 [33]	—
Al <sub>2</sub> O <sub>3</sub>	166.24	139.8	95.13	-27.02	-152.8	0.67	12.7	1.88 [57]	—
LiF	51.51	30.72	-84.74	-83.94	-87.54	0.68	5.5	5.14 [33]	—
CaF <sub>2</sub>	45.15	65.2	-135.21	-95.85	-43.69	0.75	6.14	7.0–10.4 [32]	9.3 [58]
CaWO <sub>4</sub>	40.78	57.94	—	—	—	—	—	7.9 [59]–140 [60]	—

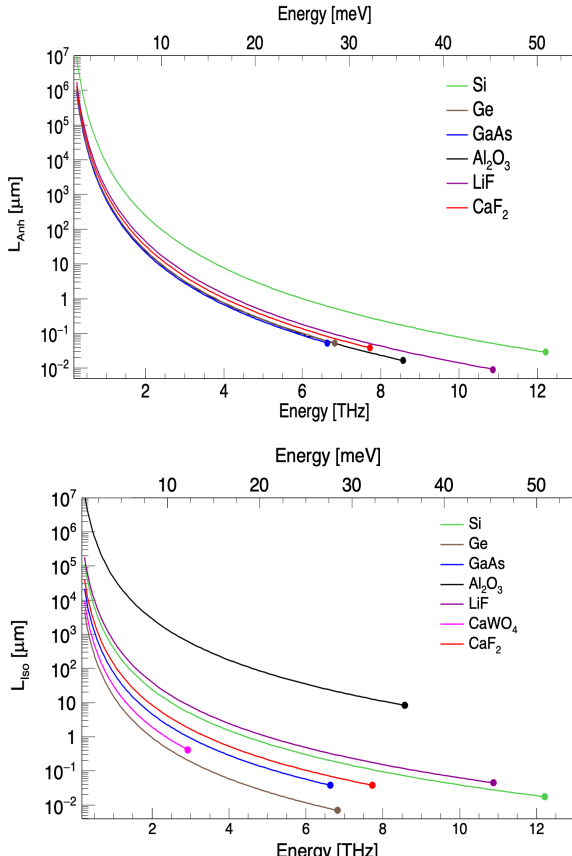


Figure 1: Characteristic length scales for anharmonic decay (top) and isotopic scattering (bottom) extracted from a cross-check simulation after implementing the calculated rate coefficients from Table 3. The dot at the right-most point of each curve represents the maximum acoustic phonon energy  $\omega_A$  extracted from table 5.

### 3.1 Results: Anharmonic Downconversion

Table 3 presents our calculations of the second- and third-order isotropic elastic coefficients and

the subsequent calculation of the parameter  $A$  in Equation 1. In these calculations, the second order elastic constants  $C_{ijkl}$  used in computing  $\mu$  and  $\lambda$  as well as the third order elastic constants  $C_{ijklmn}$  used in computing  $\alpha$ ,  $\beta$ , and  $\gamma$  can be found in Appendix A. The calculations are done assuming phonon energies of 1 THz, which are within the “low-temperature” approximation assumed for Equation 1. We also present in Table 3 two additional values,  $A_{c,l}$  and  $A_{m,l}$ , which are calculated values for  $A$  found in literature and experimentally measured values for  $A$  found in literature, respectively. In our calculations of  $A$  agree with literature calculations of  $A_{c,l}$  to within a factor of few for most materials. There is some additional disagreement for sapphire, which we attribute to two factors: the non-isotropy assumed in the calculations in Ref [57], and the steep fifth-power dependence on the assumed sound speed used to convert the results in Ref [57] into the form given in Equation 1. To the authors’ knowledge, only one of these materials has an  $A_{m,l}$  that has been measured directly: CaF<sub>2</sub>. In Ref. [58], this parameter is measured using an optical technique that is sensitive to phonon absorption by a doublet of an Eu<sup>2+</sup> dopant in the crystal that is tunable with applied stress. We leave additional discussion on experimental validation of this parameter for Section 4.

With these values calculated, we also integrate them into G4CMP and run a cross-check simulation to confirm the expected interaction rate. In this simulation, one million longitudinal acoustic phonons of varying energies are generated in a large block of material and allowed to propagate with isotopic scattering processes turned off. The block is large enough that surface interactions do not affect the phonon trajectories. For every lon-

Table 4: Isotopic scattering rates for the set of target materials of interest. We also include some inputs to the calculation that gives those rates: the lattice cell volume  $\Omega$  and the polarization-averaged cubed sound speed  $\langle c^3 \rangle$ , as well as our calculation of the mass defect coefficient  $\Gamma_{md}$ . Ranges in the  $B_{m,l}$  column correspond to measurements of different phonon polarizations. For literature values  $B_{c,l}$  and  $B_{m,l}$ , references are provided after the stated values.

Material	$\Omega$ [ $A^3$ ]	$\Gamma_{md}$	$\langle c^3 \rangle$ [ $10^{11} m^3/s^3$ ]	$B$ [ $10^{-42} s^3$ ]	$B_{c,1}$ [ $10^{-42} s^3$ ]	$B_{m,1}$ [ $10^{-42} s^3$ ]
Si	2.0	$2.02 \times 10^{-4}$	2.13	2.33	2.42	2.42-2.56 [61]
Ge	2.26	$5.88 \times 10^{-4}$	0.46	35.4	36.7 [38]	—
GaAs	2.38	$9.16 \times 10^{-5}$	0.479	7.22	7.38 [39]	5.9-29.5 [61]
Al <sub>2</sub> O <sub>3</sub>	0.5	$1.25 \times 10^{-5}$	3.06	0.025	—	0.04 [59]
LiF	0.81	$1.36 \times 10^{-4}$	1.19	1.17	1.69 [33]	—
CaF <sub>2</sub>	1.4	$1.83 \times 10^{-4}$	0.84	4.83	9.13 [62]	20.3 [62]
CaWO <sub>4</sub>	1.3	$2.02 \times 10^{-4}$	0.22	15.0	2.4 [59]-59 [60]	—

400 longitudinal phonon generated, the distance from creation point to subsequent decay is tabulated and  
401 inserted into a histogram corresponding to that  
402 phonon's energy. For each histogram, a characteristic decay length is tabulated, and that decay  
403 length appears as a function of energy in the top  
404 panel of Figure 1. In all materials tested, we find  
405 that the value of  $A$  derived from fits to these plots  
406 is consistent with the value of  $A$  used as input to  
407 G4CMP.  
408

### 3.2 Results: Isotopic Scattering

410 Table 4 presents elements of the calculation for  
411 the isotopic scattering rate coefficient  $B$  found in  
412 Equation 3. Since in the isotropic continuum ap-  
413 proximation the isotopic scattering rate simplifies  
414 to Equation 3, the main requirement is to calcu-  
415 late the mass defect coefficient  $\Gamma_{md}$  for the mate-  
416 rial. For our calculations, we assume natural abun-  
417 dances of every atom within each material consid-  
418 ered [63], which yields the values of  $\Gamma_{md}$  in the  
419 table. While isotopic enrichment of materials is  
420 possible, we present the rates from natural isotopic  
421 abundances to demonstrate a baseline strategy for  
422 how this calculation can be extended to other ma-  
423 terials of interest for integration into G4CMP.  
424

425 For isotopic scattering, we again show our own  
426 calculation of  $B$  in Table 4 accompanied by lit-  
427 erature calculations  $B_{c,l}$  and literature measure-  
428 ments  $B_{m,l}$  along with references. Here, calculated  
429 scattering rates found in literature are generally  
430 found to be within a factor of a few of our es-  
431 timates. Where there are measurements of this iso-  
432 topic scattering rate, our estimates are similarly  
433 within a factor of a few of the measured litera-  
434 ture values. Methods available in the literature  
435 have taken on three forms: thermal conductivity  
436 measurements in Ref. [62], a phonon backscat-  
437 tering technique used by Ref. [59], and a tech-  
438 nique in which phonons are scattered around a slot cut  
439 into the chip under test as in Ref. [61]. While these  
440 measurements are more commonly available than

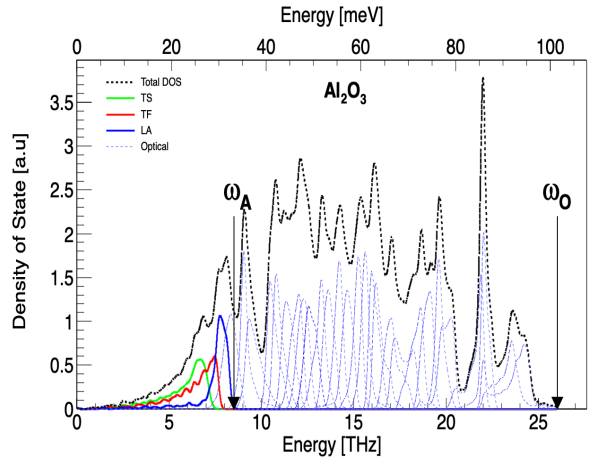


Figure 2: Contribution of phonon density of states per branch, for sapphire, showing the three acoustic branches solid lines (red, green, blue) separately and showing all optical branches in the same color (dashed blue lines). The total density of states is the dashed black line. Black solid arrows are used to indicate the maximum acoustic  $\omega_A$  and optical  $\omega_O$  phonon frequencies.

measurements of the anharmonic decay coefficient  
441  $A$ , they are nonetheless still difficult to find for all  
442 of the materials we study.  
443

444 To test isotopic scattering's implementation  
445 into G4CMP we implement the same cross-check  
446 procedure as before, but with anharmonic decay  
447 turned off within G4CMP. The results are shown  
448 in the bottom panel of Figure 1. As the isotopic  
449 scattering rate is averaged over the multiple differ-  
450 ent polarizations, this represents an average char-  
451 acteristic length for all phonon polarizations. We  
452 again find that the characteristic decay lengths are  
453 consistent with the input rates used and a  $\nu^4$  de-  
454 pendence.  
455

### 3.3 Results: Density of States

456 For each of the crystal structures we study in  
457 this work, we compute phonon dispersion curves  
458 for the various phonon branches, and use these to  
459

Table 5: Fractional density of states STDOS:FTDOS:LDOS at 1 THz, maximum acoustic phonon frequency  $\omega_A$ , maximum acoustic optical phonon frequency  $\omega_O$ , and experimental maximum optical frequency  $\omega_{OE}$ . The theoretical values are obtained using phonopy [45]. The rightmost column provides references for the  $\omega_{OE}$  column’s values. Due to limited availability of Phonopy input files for Ge, the values quoted here for Ge are from Refs. [26, 64], and are not new calculations.

Material	STDOS:FTDOS:LDOS	$\omega_A$ [THz]	$\omega_O$ [THz]	$\omega_{OE}$ [THz]	Refs.
Si	0.521 : 0.406 : 0.071	12.14	15.28	15.5	[64]
Ge	0.535 : 0.366 : 0.097	6.63	9.02	9.02	[64]
GaAs	0.584 : 0.337 : 0.078	6.56	8.58	8.82	[65]
$\text{Al}_2\text{O}_3$	0.511 : 0.351 : 0.137	8.41	26.29	26.35	[66]
LiF	0.5156 : 0.386 : 0.0983	10.73	18.19	19.7	[67]
$\text{CaF}_2$	0.599 : 0.318 : 0.0819	7.55	13.65	13.67	[68]
$\text{CaWO}_4$	0.475 : 0.408 : 0.115	2.72	25.94	26.07	[69]

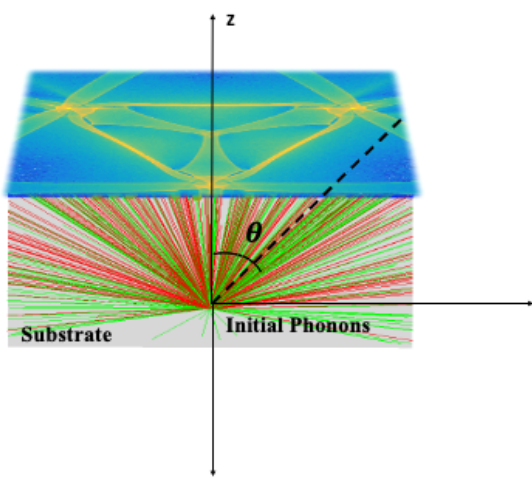


Figure 3: A rendering of the simulation to test G4CMP’s propagation along caustics. The gray box is the substrate (sapphire, in this image), the red lines are transverse fast phonon trajectories, the green lines are the transverse slow phonon trajectories, and  $\theta$  is the angular scan range. The blue rectangle on the top surface of the substrate is the phonon collection plane, where brighter colors indicate more densely concentrated phonon impacts. Here, phonons were generated at the bottom of the substrate.

construct branch-specific density of states curves as a function of energy (Figure 2). Fractional density of states contributions are then computed for acoustic longitudinal, fast transverse, and slow transverse phonons at 1 THz, with the results shown in Table 5. These values are used as inputs to G4CMP. Energy-dependent DOS curves are shown for additional materials in Appendix B.

### 3.4 Results: Propagation along Caustics

To demonstrate successful implementation of the physical processes responsible for phonon propagation along caustics, we compare simulated caustic patterns against experimental heat-pulse caustic measurements. For each material, we cre-

ate a simple G4CMP geometry consisting of a 2mm cube of substrate with its  $+z$  face acting as a phonon collection plane (Figure 3). Anharmonic downconversion and isotopic scattering are turned off to have ballistic phonons. 40 million low-energy phonons (at 1 THz) are simulated isotropically from a point at  $x = 0$ ,  $y = 0$ , and a  $z$  chosen to ensure that the collecting plane subtends the same angular scan range  $\theta$  as those reported in experimental caustics probes. The locations of phonons landing on the collection plane are recorded, and histogrammed. The ratio of longitudinal to transverse-fast to transverse-slow polarizations used here is 0:1:1. This ratio is used primarily for comparison with the experimental data (see below), which often uses arrival-time-based gates to select the transverse phonon signal and cut away the longitudinal signal.<sup>5</sup> The top panel in Figure 4 (Figure 5) shows the resulting caustic patterns for sapphire, with the crystal direction [1102] ([0010]) oriented out of the page. We also show simulated caustics for GaAs (Figure 6), LiF (Figure 7),  $\text{CaWO}_4$  (Figure 8), and  $\text{CaF}_2$  (Figure 9).

We validate our simulations against experimental caustics measurements from literature, shown in the bottom panels of Figures 4-9. Phonon caustics imaging has been achieved in a variety of materials, including all of the materials shown in Table 3. Such experiments typically proceed as follows. A crystal substrate under test is outfitted with a small, single bolometer (area  $\simeq 50\mu\text{m} \times 50\mu\text{m}$ ) on one side and a metal film on the other, and is then cooled to cryogenic temperatures (few K scale or below). A phonon burst is then produced at cryogenic temperatures by passing a short burst of current through the metal film

<sup>5</sup>It is also worth noting that the longitudinal phonon signal commonly shows less pronounced caustic structures than transverse phonon signals in a variety of materials, often displaying only a central “hotspot” of detected phonons in such images.

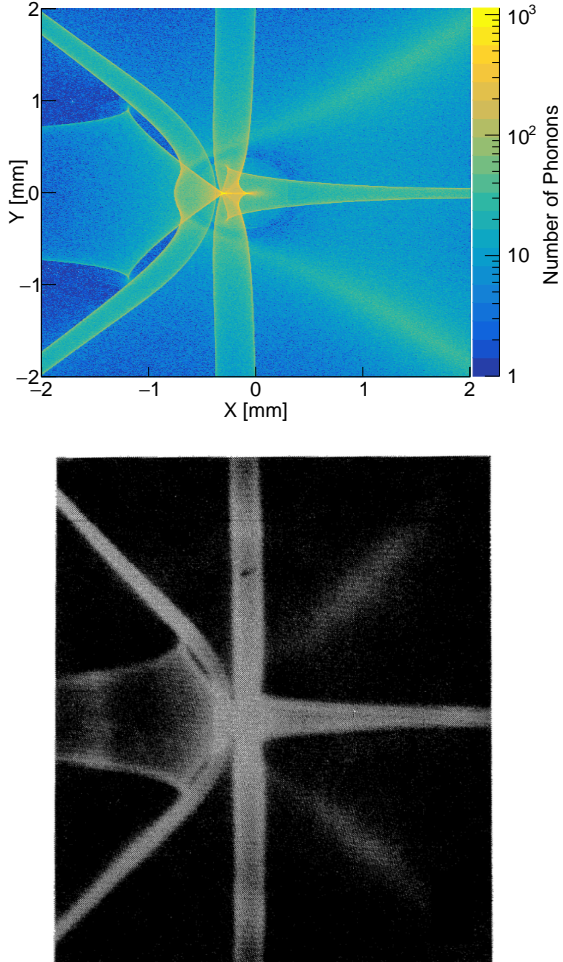


Figure 4: Top: phonon caustic image for sapphire ( $\text{Al}_2\text{O}_3$ ) obtained from G4CMP. The crystal direction  $[1\bar{1}02]$  is at the center of the pattern, oriented out-of-page. Bright regions indicate directions of high phonon flux. Bottom: phonon caustic image for sapphire measured at 1.6 K in Ref. [70], where the crystal direction  $[1\bar{1}02]$  is out of page and horizontal scan range is  $\pm 32^\circ$ . This angular scan range matches that used in our simulations

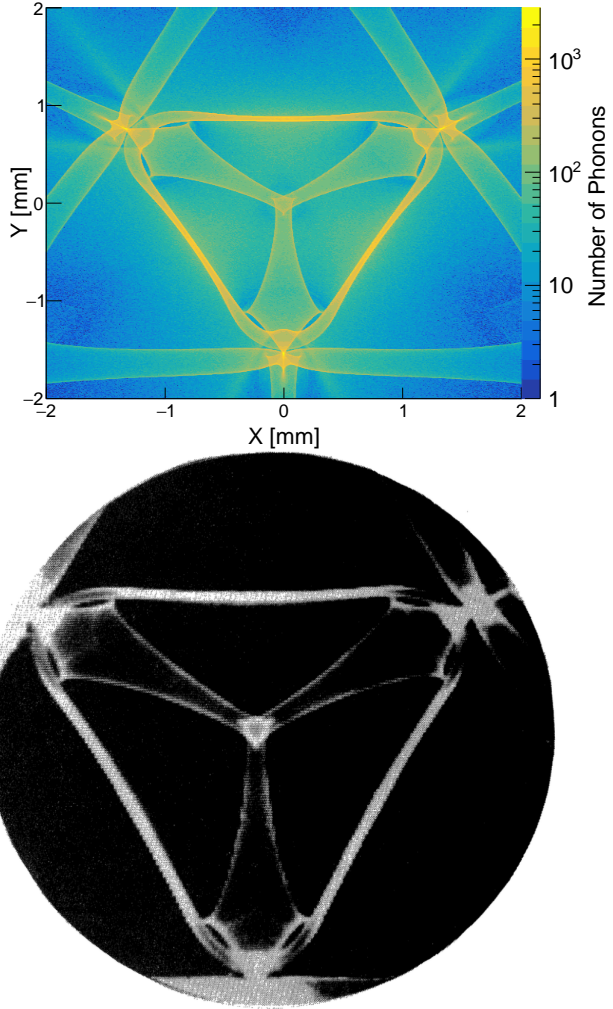


Figure 5: Top: phonon caustic image for sapphire ( $\text{Al}_2\text{O}_3$ ) obtained from G4CMP. The crystal direction  $[0010]$  is at the center of the pattern, oriented out-of-page. Bottom: phonon caustic image for sapphire measured at 1.6 K in Ref. [70], where the crystal direction  $[0010]$  is out of page and horizontal scan range is  $\pm 58^\circ$ .

511 or by illuminating the metal film locally with laser  
 512 light. In this process, several non-spherical shells  
 513 of longitudinal and transverse phonons are pro-  
 514 duced locally. Of these locally-created phonons,  
 515 only those traveling in the direction of the bolome-  
 516 ter are detected. While this experimental data-  
 517 taking scheme is geometrically different from our  
 518 simulation, functionally the mappings are identi-  
 519 cal: the pattern of phonons radiated from a point  
 520 onto a surface (collecting plane) should be the  
 521 same as the pattern of phonons radiated from  
 522 an extended surface onto a point (bolometer).  
 523 This enables direct comparisons between the simu-  
 524 lated and experimentally-acquired images of these  
 525 phonon caustics. In the comparisons we present,  
 526 exact normalization of the different polarization  
 527 components is not known for many of the experi-

528 mental images, but in most<sup>6</sup> cases the phonon im-  
 529 ages have been time-gated to select only transverse  
 530 phonons. We therefore attempt to coarsely match  
 531 this weighting of polarizations by using a 0:1:1 ra-  
 532 tio for L:TF:TS phonons, but acknowledge that  
 533 this may not yield a perfect match to the relative  
 534 amplitudes of the measured caustic signals.

535 Even despite this uncertainty in the polarization  
 536 weighting, the shapes of the resulting caustic  
 537 images constructed with G4CMP and the shapes  
 538 of the corresponding experimental images agree  
 539 well, given the identical lateral scan ranges. This  
 540 implies successful integration of these new mate-  
 541 rials' phonon transport properties into G4CMP.  
 542 Direct quantitative comparisons of the brightness

<sup>6</sup>NB: Ref. [55] does not specify if these are time-gated to select only transverse phonons.

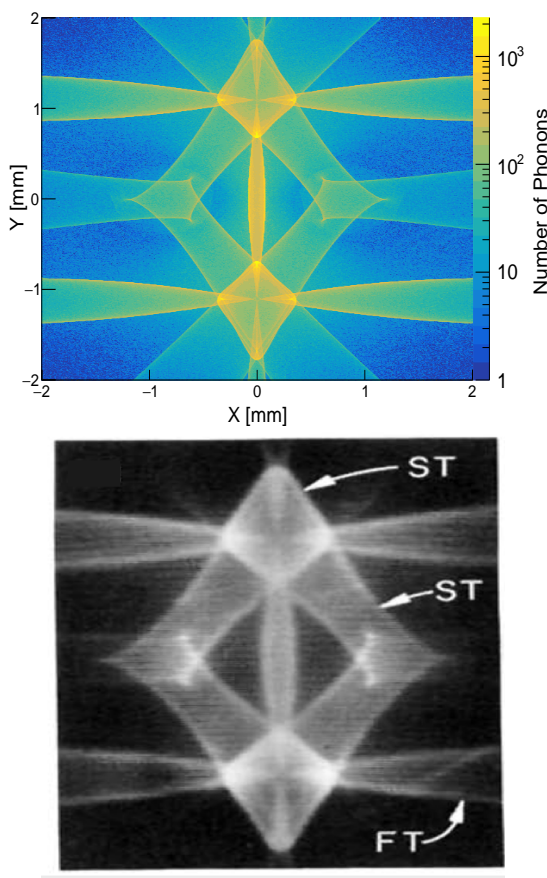


Figure 6: Top: phonon caustic image for GaAs obtained from G4CMP. The crystal direction [110] is at the center of the pattern, oriented out-of-page. Bottom: phonon caustic image for GaAs measured at 1.8 K in Ref. [71], where the crystal direction [110] is out of page and horizontal scan range is  $\pm 59^\circ$ .

of different regions is challenging given the format of the literature data and the unknown degree to which the experimental response displays a saturation in intensity. For this reason, we focus on shape comparisons.<sup>7</sup>

It is worth noting that many of the studies from which we've obtained the experimental images also perform caustic simulations which show good agreement with their experimental results. However, to the authors' knowledge, these simulations have largely been done with separate custom simulation software dedicated to exploring caustics. This current work is not only a demonstration of a framework that we can use to reproduce similar results within a single public-facing software package, but also that we can do so within

<sup>7</sup>This also contributes to our decision to display our plots with a logarithmic intensity (z)-axis: even though they are less comparable to the literature heat-pulse images, such logarithmic plots give more insight into the caustic structures than what is available in the sometimes-saturated experimental images.

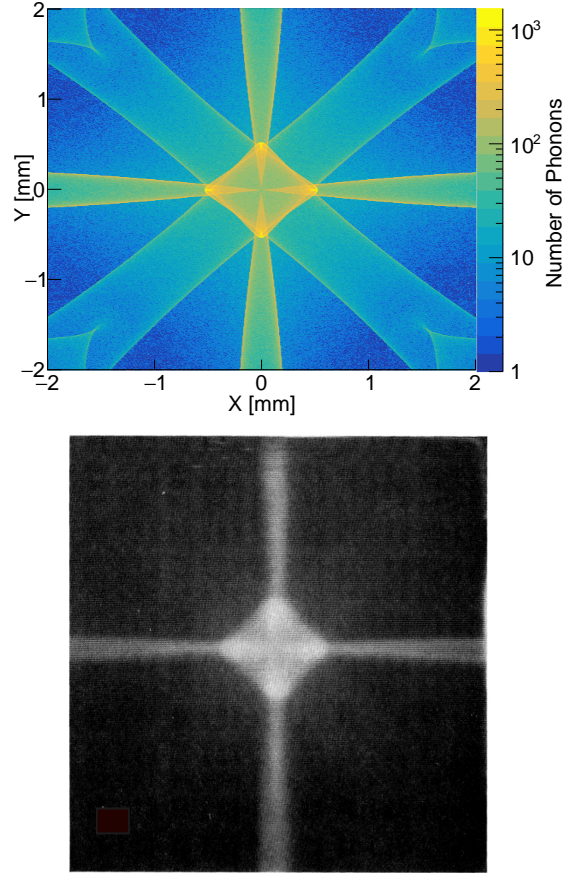


Figure 7: Top: phonon caustic image for LiF obtained from G4CMP. The crystal direction [100] is at the center of the pattern, oriented out-of-page. Bottom: phonon caustic image for LiF measured at 2.2 K in Ref. [72], where the crystal direction [100] is out of page and horizontal scan range is  $\pm 40^\circ$ .

a package whose primary goal is an application of this physics to understanding low-energy detector response.

## 4 Discussion

The primary goal of this work has been to present and demonstrate a streamlined framework for integrating new materials into the G4CMP low-energy simulation software. The striking agreement between simulated and measured caustic diagrams for sapphire, LiF, GaAs, CaWO<sub>4</sub>, and CaF<sub>2</sub> illustrate the general success of this implementation, and the relatively small set of required parameters needed for modeling this phonon transport within a publicly available software package. Moreover, the similar simplicity in input parameters for modeling anharmonic decay and isotopic scattering continues to paint an encouraging picture of accessibility for efforts to model phonon transport in future novel detector materials.

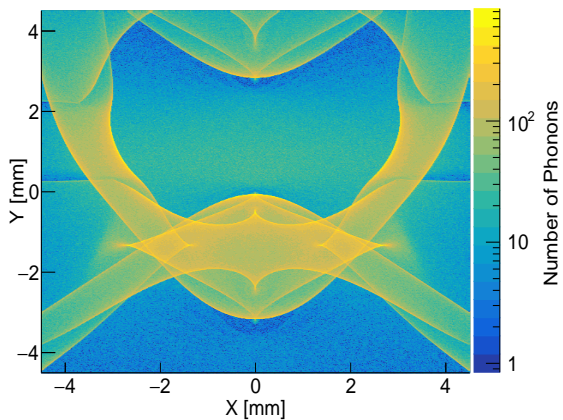


Figure 8: Top: phonon caustic image for  $\text{CaWO}_4$  obtained from G4CMP. The crystal direction [010] is at the center of the pattern, oriented out-of-page. Bottom: phonon caustic image for  $\text{CaWO}_4$  measured below 2 K in Ref. [55], where the crystal direction [010] is out of page and horizontal scan range is  $\pm 56.3^\circ$ . In the simulation used to produce the top image, the crystal has been laterally extended to 9.1 mm square and 3 mm thick to enable a match to the scan range from the (bottom) experimental data.

Given this modeling success, three natural topics of future interest are how one can further improve G4CMP’s modeling capabilities, what work needs to be done to validate these models, and how this framework plays a role in particle detection and QIS applications.

From this work, we identify a few areas where future effort could be reasonably made to further improve realism in G4CMP’s phonon modeling. First, the calculations here could be redone without using the isotropic continuum approximation in modeling downconversion and isotopic scattering. In G4CMP, the rates of these processes are agnostic to the direction of the decaying/scattering phonon. Ref. [32] demonstrates not only that the rates of phonon downconversion vary by factors of a few depending on the direction of propagation, but also that in a rigorously-modeled anisotropic scenario, more decay modes are possible than the  $L \rightarrow T + T$  and  $L \rightarrow L + T$  that G4CMP currently models: both transverse fast and transverse

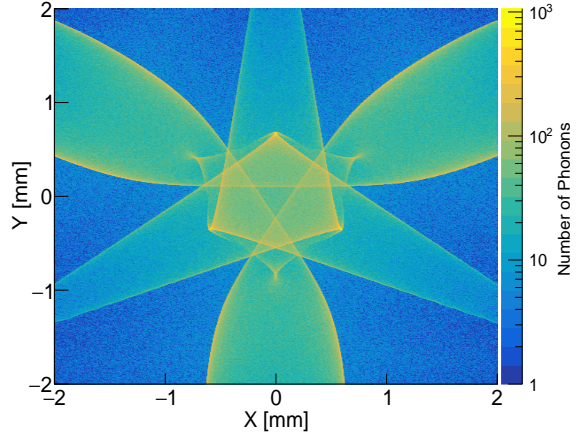


Figure 9: Top: phonon caustic image for  $\text{CaF}_2$  obtained from G4CMP. The crystal direction [111] is at the center of the pattern, oriented out-of-page. Bottom: phonon caustic image for  $\text{CaF}_2$  measured in Ref. [73], where the crystal direction [111] is out of page and horizontal scan range is  $\pm 23^\circ$ . No measurement temperature was reported.

slow phonons may undergo anharmonic decay. As G4CMP preserves the phonon direction and polarization information step-by-step, a natural extension of this work may therefore be to implement this direction-dependence and more complex polarization dependence of rate. Furthermore, while phonon scattering on isotopic impurities is handled as being isotropic in momentum ( $k$ -)space according to G4CMP, this is not universally true: experiments in Ref [61] indicate that there is also a degree of anisotropy to be expected in the phonon scattering process, beyond that incurred from just propagation along caustics from the scattering site. Second, an improvement to G4CMP may include accounting for dispersion’s impact on the phonon caustics, which currently do not (but should) change as a function of phonon energy [54]. This energy dependence may also be responsible for small degrees of disagreement observed between simulated and measured caustics patterns in Figures 4–9. Other improvements to G4CMP include modeling electron/hole trans-

621 port and processes in these newly-added materials,  
622 adding photon interactions with the substrate,  
623 and developing functionality for quanta to tra-  
624 versate boundaries between different crystals (such  
625 as the interface between a substrate and its super-  
626 conducting film). While a thorough discussion of  
627 these efforts is beyond the scope of this work, they  
628 will be the topic of follow-up studies.

629 This work has also highlighted strategies used  
630 to validate phonon transport models in our ex-  
631 panded set of target materials, as well as the  
632 fact that measurements are still needed to per-  
633 form this validation for many of the materials con-  
634 sidered. Measurements of the anharmonic decay  
635 rate coefficient,  $A_{m,l}$ , are largely absent: we were  
636 only able to find one direct measurement  $A_{m,l}$  for  
637  $\text{CaF}_2$ . This direct measurement relies on doping  
638 a crystal with  $\text{Eu}^{2+}$  atoms and taking advantage  
639 of the stress-dependence of optical transitions in  
640 that atom. Employing this strategy in an arbit-  
641 rary material clearly runs into prohibitive chal-  
642 lenges when the material bandgap is lower than the  
643 energy of the optical transitions accessible, which  
644 may help explain why  $A_{m,l}$  has not been measured  
645 (to the authors' knowledge) for any of the optically  
646 opaque materials studied here. This strategy may  
647 be viable for directly measuring anharmonic de-  
648 cay rates in other optically clear materials, but  
649 it is unclear how broadly applicable it may be  
650 in validating estimates of  $A$  for arbitrary materi-  
651 als. Another possible (albeit less direct) means of  
652 measuring this may follow the heat-pulse strategy  
653 employed in Ref. [59]. Here, heat pulse transmis-  
654 sion measurements are taken at cryogenic temper-  
655 atures using a bolometer, and for sufficiently large  
656 heater powers, they are (plausibly) affected by an-  
657 harmonic downconversion in the material. While  
658 such measurements are also affected by isotopic  
659 scattering and would have to simultaneously fit for  
660 both  $A$  and  $B$ , they nonetheless may grant some  
661 sensitivity to directly measuring downconversion  
662 rates. The isotopic scattering rate  $B$  seems more  
663 straightforward to measure than  $A$ , which may be  
664 partly due to the more diverse set of measurement  
665 techniques cited in Table 4. However, we were still  
666 not able to find a measured isotopic scattering rate  
667 coefficient  $B_{m,l}$  for all materials. Overall, these ob-  
668 servations illustrate that most materials are miss-  
669 ing measurements of fundamental phonon trans-  
670 port parameters needed for validation of transport  
671 models in our expanded set of materials.

672 Lastly, it is worth discussing how the tools de-  
673 veloped here strengthen particle detection and QIS  
674 applications. While we used this framework to  
675 model several new materials, it can be readily ex-  
676 tended in kind to arbitrary solid-state materials  
677 that are well-motivated from low-threshold sensing  
678 and QIS standpoints. Diamond,  $\text{SiO}_2$  and  $\text{AlN}$  are

particular well-motivated dark matter targets  
679 as they are advantageous for looking for single-  
680 phonon excitations produced from a DM interac-  
681 tion through a hydrophilic scalar mediator [47].  
682 Other materials like  $\text{SiC}$  are also well-motivated as  
683 DM targets, as they may enable sensitive probes of  
684 a broad set of DM models [74]. Other more com-  
685 plex crystals with low electronic bandgaps such as  
686  $\text{Eu}_5\text{In}_2\text{Sb}_6$  are also of current interest for their low-  
687 ered threshold (relative to Si and Ge) for charge  
688 readout [75]. If those are also used in an NTL  
689 phonon-amplification and sensing scheme, being  
690 able to understand phonon propagation within  
691 them will also be critical for detector response  
692 modeling. Other materials such as  $\text{Li}_2\text{MoO}_4$  and  
693  $\text{TeO}_2$  might also modeled to the benefit of the neu-  
694 trinoless double beta decay communities, where  
695 detector energy resolution, not detector energy  
696 threshold, is commonly prioritized [76, 77]. From  
697 a QIS perspective, Si and  $\text{Al}_2\text{O}_3$  are the most com-  
698 mon substrates used, and are now both modeled  
699 in G4CMP. However, superconductors such as alu-  
700 minum, niobium, and tantalum are all commonly  
701 used in ground plane and circuit design. Coupling  
702 this framework (applied to those materials)  
703 with an expansion of G4CMP's ability to transport  
704 phonons between different crystals will enable rig-  
705 orous characterization of microphysics in the su-  
706 perconducting layer, which is important for mod-  
707 eling quasiparticle-induced qubit errors. Though  
708 it is beyond the scope to discuss and analyze  
709 all well-motivated materials candidates for sens-  
710 ing and QIS, the framework presented here will  
711 enable more efficient modeling of these materials  
712 in G4CMP.  
713

714 The results of this work may provide additional  
715 use in applications where particle impacts are ex-  
716 pected to be spatially localized within a device. In  
717 such a scenario, these phonon models (and notably  
718 caustic patterns) may enable one to place sensors  
719 to maximize the chances of observing the emergent  
720 phonon pulses created from the impact point [26].  
721 As more materials' phonon transport properties  
722 are integrated into G4CMP, such strategies may  
723 be more easily used to improve a device's detection  
724 efficiency. Overall, this framework's general assis-  
725 tance in understanding a material's microphysical  
726 phonon response provides the foundation for mod-  
727 eling signal and background responses in a dark  
728 matter direct detection experiment and for mod-  
729 eling phonon-induced correlated errors in super-  
730 conducting qubits.

## 5 Conclusion

731  
732 In this work, we have presented a condensed  
733 framework for adding phonon transport modeling

734 into the G4CMP simulation package for new materials of interest to the dark matter direct detection and QIS communities. We have used this  
 735 framework to explore phonon transport parameters needed by G4CMP for seven materials, five  
 736 of which have not yet been integrated into a comprehensive low-energy simulation package: GaAs,  
 737  $\text{Al}_2\text{O}_3$ , LiF,  $\text{CaWO}_4$ , and  $\text{CaF}_2$ . Moreover, we  
 738 have accompanied this exploration with a literature search of calculated and measured phonon  
 739 transport parameters for those materials, and have found that the integration of our calculations into  
 740 G4CMP gives phonon propagation that is largely consistent with calculated and/or measured decay  
 741 rates, scattering rates, phonon density of states,  
 742 and phonon caustics in those materials. As measurements for all materials were not found in this  
 743 search, it is also apparent that there is further  
 744 need for experimental work to help validate these  
 745 phonon transport parameters for many materials  
 746 of interest.

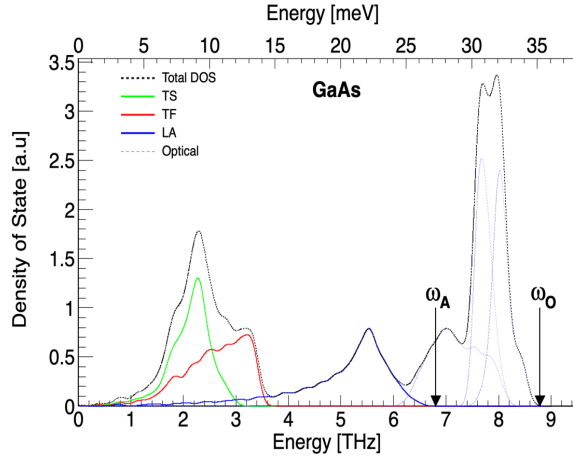
## 755 6 Acknowledgements

756 The authors would like to thank Tanner Trickle  
 757 for providing insights and suggesting strategies for  
 758 calculating the density of states for various materials.  
 759 Finally, we thank the rest of the Fermilab  
 760 QSC group for freeing up person-hours for the  
 761 authors to develop this work. This manuscript has  
 762 been authored by Fermi Research Alliance, LLC  
 763 under Contract No. DE-AC02-07CH11359 with  
 764 the U.S. Department of Energy, Office of Science,  
 765 Office of High Energy Physics. This work was sup-  
 766 ported by the U.S. Department of Energy, Office  
 767 of Science, National Quantum Information Science  
 768 Research Centers, Quantum Science Center and  
 769 the U.S. Department of Energy, Office of Science,  
 770 High-Energy Physics Program Office.

771 IH led the development of the work presented  
 772 in this paper. RL and RK provided supporting  
 773 checks to calculations in this work and shaped  
 774 the narrative of the manuscript. RL, RK, and IH  
 775 drafted the manuscript. EFF and LH provided  
 776 regular feedback over the course of the included  
 777 work. All authors helped in preparation of this  
 778 paper on the presented result.

## 779 Appendix A Elastic Constants

780 In Table A.6 we provide numerical values of the  
 781 elastic constants used in this work. The second-  
 782 order elastic constants are used to model caustic  
 783 propagation, and are also used to calculate the  
 784 second-order parameters  $\mu$  and  $\lambda$  needed for calcu-  
 785 lation of the anharmonic decay coefficient  $A$ . The  
 786 third-order elastic constants are used in finding  $\alpha$ ,



787 Figure B.10: Partial density of states of GaAs for transverse slow (green), transverse fast (red) and longitudinal (blue)  
 788 acoustic phonons (solid lines). The blue dashed curves to  
 789 the right of the acoustic curves show the partial contribution  
 790 of optical phonon channels to the DOS. The total density of states is the black line.  $\omega_A$  corresponds to the  
 791 maximum acoustic phonon energy and  $\omega_O$  is the maximum  
 792 optical phonon energy.

793  $\beta$ , and  $\gamma$ , also needed for calculating the anhar-  
 794 monic decay coefficient. All coefficients are given  
 795 in (pressure) units of GPa. Sources for the elas-  
 796 tic constants are found in the rightmost column.  
 797 Standard third-order elastic constants for  $\text{CaWO}_4$   
 798 were not found.

## Appendix B Density of States

799 We display phonon density of states curves for  
 800 GaAs (Figure B.10), LiF (Figure B.11), and  $\text{CaF}_2$   
 801 (Figure B.12). These curves have significantly re-  
 802duced complexity in their optical branches relative  
 803 to  $\text{Al}_2\text{O}_3$  due to the smaller number of atoms in  
 804 a unit cell. The Debye Frequency  $\omega_O$  is used in  
 805 G4CMP. The jitter in the DOS values at energies  
 806 below approximately 5 THz is due to low-statistics  
 807 in the numbers of points computed during the dis-  
 808 perspersion calculation. However, for LDOS, FT DOS,  
 809 and STDOS values in Table 5, a separate simula-  
 810 tion with increased  $\vec{k}$ -space point density was used  
 811 to avoid these fluctuations.

## References

- [1] A. Arbey, F. Mahmoudi, [Dark matter and the early universe: A review](#), Progress in Particle and Nuclear Physics 119 (2021) 103865. [doi:<https://doi.org/10.1016/j.ppnp.2021.103865>](https://doi.org/10.1016/j.ppnp.2021.103865). URL <https://www.sciencedirect.com/science/article/pii/S0146641021000193>
- [2] D. H. Weinberg, J. S. Bullock, F. Governato, R. Kuzio de Naray, A. H. G. Peter, [Cold dark matter: Controversies on small scales](#), Proceedings of the National Academy of Sciences 112 (40) (2015) 12249–12255. [doi:\[10.1073/pnas.1308716112\]\(https://doi.org/10.1073/pnas.1308716112\)](https://doi.org/10.1073/pnas.1308716112). URL <http://dx.doi.org/10.1073/pnas.1308716112>

Table A.6: Values of the second and third-order elastic constants in units of pressure (GPa) used in the calculation for anharmonic downconversion.

Material	Second-order C <sub>11</sub> ,C <sub>12</sub> ,C <sub>44</sub> [GPa]	Third-order C <sub>111</sub> ,C <sub>112</sub> ,C <sub>123</sub> ,C <sub>144</sub> ,C <sub>166</sub> ,C <sub>456</sub> [GPa]	Refs.
Si	[167.8,65.2,80.1]	[-880,-515,27,74,-385,-40]	[31]
Ge	[126,44.67]	[-760,-410,-70,0,-310,-46]	[78]
GaAs	[121.1,57.4,59.5]	[-620,-392,-62.8,-274.3,-43]	[54]
CaF <sub>2</sub>	[174.5,56.4,35.93]	[-1246,-400,-254,-124,-214,-75]	[79]
LiF	[111.2,42.0,62.8]	[-1646,-252,92,98,-261,97]	[80]
Second-order C <sub>11</sub> ,C <sub>12</sub> ,C <sub>13</sub> ,C <sub>14</sub> ,C <sub>34</sub> ,C <sub>44</sub> [GPa]		Third-order C <sub>111</sub> ,C <sub>112</sub> ,C <sub>113</sub> ,C <sub>114</sub> ,C <sub>123</sub> ,C <sub>124</sub> ,C <sub>133</sub> ,C <sub>134</sub> , C <sub>144</sub> ,C <sub>155</sub> , C <sub>222</sub> ,C <sub>333</sub> ,C <sub>344</sub> ,C <sub>444</sub> [GPa]	
Al <sub>2</sub> O <sub>3</sub>	[495, 161.1, 111.1, -22.2, 499.9,-147.7]	[-394.6,-112.7,-91.9,8.1,-20.4,-5.5,-96.4,-7.8,-38.2,-106.2,-453.4,-312.8,-113.1,4.1]	[53, 81]
Second-order C <sub>11</sub> ,C <sub>12</sub> ,C <sub>13</sub> ,C <sub>16</sub> ,C <sub>33</sub> ,C <sub>44</sub> ,C <sub>66</sub> [GPa]		Third-order C <sub>111</sub> ,C <sub>112</sub> ,C <sub>113</sub> , C <sub>123</sub> ,C <sub>133</sub> ,C <sub>114</sub> ,C <sub>155</sub> ,C <sub>166</sub> ,C <sub>333</sub> , C <sub>344</sub> ,C <sub>366</sub> , C <sub>456</sub> [GPa]	
CaWO <sub>4</sub>	[151.5,65.6,45,18.8,134,35.4,40]	—	[82]

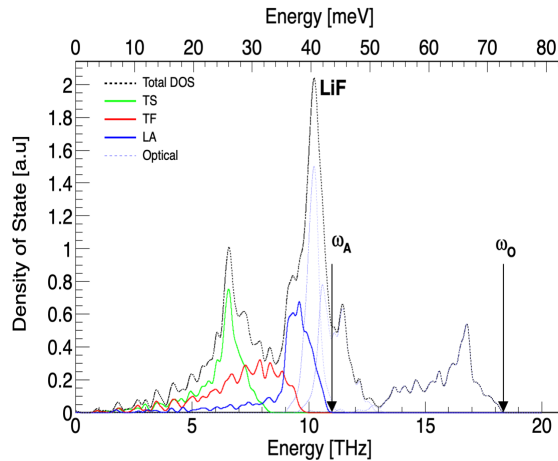


Figure B.11: Partial density of states of LiF for transverse slow (green), transverse fast (red) and longitudinal (blue) acoustic phonons (solid lines). The blue dashed curves to the right of the acoustic curves show the partial contribution of optical phonon channels to the DOS. The total density of states is the black line.  $\omega_A$  corresponds to the maximum acoustic phonon energy and  $\omega_O$  is the maximum optical phonon energy.

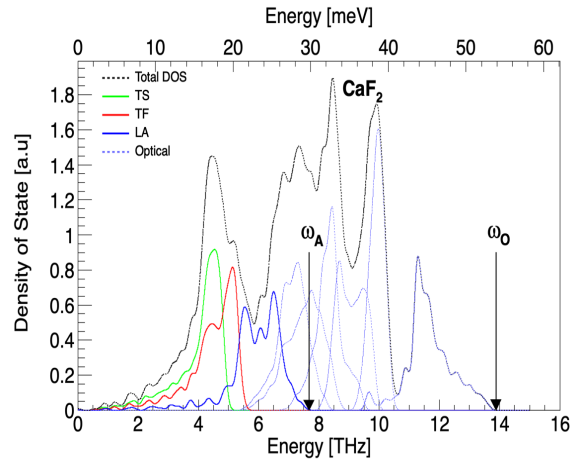


Figure B.12: Partial density of states of CaF<sub>2</sub> for transverse slow (green), transverse fast (red) and longitudinal (blue) acoustic phonons (solid lines). The blue dashed curves to the right of the acoustic curves show the partial contribution of optical phonon channels to the DOS. The total density of states is the black line.  $\omega_A$  corresponds to the maximum acoustic phonon energy and  $\omega_O$  is the maximum optical phonon energy.

- 820 [3] N. Aghanim, et al., [Planck2018 results: Vi. cosmological parameters](#), Astronomy amp; Astrophysics 641  
821 (2020) A6. doi:[10.1051/0004-6361/201833910](https://doi.org/10.1051/0004-6361/201833910).  
822 URL <http://dx.doi.org/10.1051/0004-6361/201833910>
- 823 [4] J. Aalbers, et al., A search for new physics in low-  
824 energy electron recoils from the first 1z exposure  
825 (2023). arXiv:[2307.15753](https://arxiv.org/abs/2307.15753).
- 826 [5] C. Bartram, et al., [Search for invisible axion dark matter in the 3.3 – –4.2 μeV mass range](#), Phys. Rev. Lett. 127 (2021) 261803.  
827 doi:[10.1103/PhysRevLett.127.261803](https://doi.org/10.1103/PhysRevLett.127.261803).  
828 URL <https://link.aps.org/doi/10.1103/PhysRevLett.127.261803>
- 829 [6] R. Essig, et al., [Snowmass2021 Cosmic Frontier: The landscape of low-threshold dark matter di-](#)

- rect detection in the next decade
- 830 arXiv e-prints (2022) arXiv:2203.08297 arXiv:[2203.08297](https://arxiv.org/abs/2203.08297), doi:[10.48550/arXiv.2203.08297](https://doi.org/10.48550/arXiv.2203.08297).
- 831 [7] C. W. Fink, S. L. Watkins, T. Aramaki, P. L. Brink,  
832 S. Ganjam, B. A. Hines, M. E. Huber, N. A. Kurinsky,  
833 R. Mahapatra, N. Mirabolfathi, W. A. Page, R. Par-  
834 tridge, M. Platt, M. Pyle, B. Sadoulet, B. Serfass,  
835 S. Zuber, [Characterizing tes power noise for future single optical-phonon and infrared-photon detectors](#), AIP Advances 10 (8) (Aug. 2020). doi:[10.1063/5.0011130](https://doi.org/10.1063/5.0011130).  
836 URL <http://dx.doi.org/10.1063/5.0011130>
- 837 [8] D. J. Temples, et al., Performance of a kinetic inductance phonon-mediated detector at the nexus cryo-  
838 genic facility (2024). arXiv:[2402.04473](https://arxiv.org/abs/2402.04473).
- 839 [9] R. Linehan, I. Hernandez, D. J. Temples, S. Q. Dang,  
840

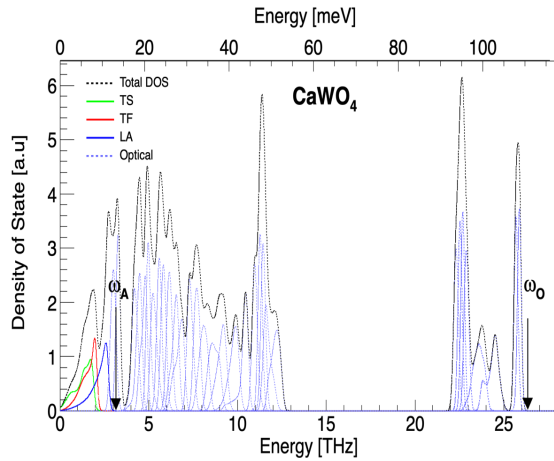


Figure B.13: Partial density of states of  $\text{CaWO}_4$  for transverse slow (green), transverse fast (red) and longitudinal (blue) acoustic phonons (solid lines). The blue dashed curves to the right of the acoustic curves show the partial contribution of optical phonon channels to the DOS. The total density of states is the black line.  $\omega_A$  corresponds to the maximum acoustic phonon energy and  $\omega_O$  is the maximum optical phonon energy.

- 852 D. Baxter, L. Hsu, E. Figueroa-Feliciano, R. Khatiwada,  
 853 K. Anyang, D. Bowring, G. Bratrud, G. Canelejo,  
 854 A. Chou, R. Gaultieri, K. Stifter, S. Sussman, Estimating  
 855 the energy threshold of phonon-mediated superconducting qubit detectors operated in an energy-  
 856 relaxation sensing scheme (2024). [arXiv:2404.04423](https://arxiv.org/abs/2404.04423).
- [10] C. W. Fink, C. P. Salemi, B. A. Young, D. I. Schuster, N. A. Kurinsky, The Superconducting Quasiparticle-Amplifying Transmon: A Qubit-Based Sensor for meV Scale Phonons and Single THz Photons (10 2023). [arXiv:2310.01345](https://arxiv.org/abs/2310.01345).
- [11] P. N. Luke, Voltage-assisted calorimetric ionization detector, Journal of Applied Physics 64 (12) (1988) 6858–6860. [arXiv:https://pubs.aip.org/aip/jap/article-pdf/64/12/6858/18621786/6858\\_1\\_online.pdf](https://arxiv.org/abs/https://pubs.aip.org/aip/jap/article-pdf/64/12/6858/18621786/6858_1_online.pdf), doi:10.1063/1.341976. URL <https://doi.org/10.1063/1.341976>
- [12] B. S. Neganov, V. N. Trofimov, Possibility of producing a bulky supersensitive thermal detector at a temperature close to absolute zero, 28 (1978) 356. URL [http://jetpletters.ru/ps/0/article\\_24160.shtml](http://jetpletters.ru/ps/0/article_24160.shtml)
- [13] M. F. Albakry, et al., First measurement of the nuclear-recoil ionization yield in silicon at 100 ev, Phys. Rev. Lett. 131 (2023) 091801. doi:10.1103/PhysRevLett.131.091801. URL <https://link.aps.org/doi/10.1103/PhysRevLett.131.091801>
- [14] M. F. Albakry, et al., Ionization yield measurement in a germanium cdmslite detector using photo-neutron sources, Phys. Rev. D 105 (2022) 122002. doi:10.1103/PhysRevD.105.122002. URL <https://link.aps.org/doi/10.1103/PhysRevD.105.122002>
- [15] R. Agnese, et al., Search for low-mass dark matter with cdmslite using a profile likelihood fit, Physical Review D 99 (6) (Mar. 2019). doi:10.1103/physrevd.99.062001. URL <http://dx.doi.org/10.1103/PhysRevD.99.062001>
- [16] R. Agnese, et al., Projected sensitivity of the supercdms snolab experiment, Physical Review D 95 (8) (Apr. 2017). doi:10.1103/physrevd.95.082002. URL <http://dx.doi.org/10.1103/PhysRevD.95.082002>

- 082002 896  
 [17] A. H. Abdelhameed, et al., First results from the cresst-iii low-mass dark matter program, Phys. Rev. D 100 (2019) 102002. doi:10.1103/PhysRevD.100.102002. URL <https://link.aps.org/doi/10.1103/PhysRevD.100.102002> 897  
 898  
 899  
 900  
 901  
 902  
 [18] K. Ishidoshiro, T. Kobayashi, K. Hosokawa, Y. Kawamura, Y. Kamei, S. Mima, C. Otani, A. A. Suzuki, M. Zulfakri, T. Taino, Kinetic inductance detectors on calcium fluoride substrate for astroparticle physics, Progress of Theoretical and Experimental Physics 2023 (10) (2023) 103H02. [arXiv:https://academic.oup.com/ptep/article-pdf/2023/10/103H02/52713177/ptad124.pdf](https://academic.oup.com/ptep/article-pdf/2023/10/103H02/52713177/ptad124.pdf), doi:10.1093/ptep/ptad124. URL <https://doi.org/10.1093/ptep/ptad124> 903  
 904  
 905  
 906  
 907  
 908  
 909  
 910  
 911  
 912  
 913  
 914  
 915  
 916  
 917  
 [19] S. Griffin, S. Knapen, T. Lin, K. M. Zurek, Directional detection of light dark matter with polar materials, Physical Review D 98 (11) (Dec. 2018). doi:10.1103/physrevd.98.115034. URL <http://dx.doi.org/10.1103/PhysRevD.98.115034> 918  
 919  
 920  
 921  
 922  
 923  
 [20] S. Knapen, T. Lin, M. Pyle, K. M. Zurek, Detection of light dark matter with optical phonons in polar materials, Physics Letters B 785 (2018) 386–390. doi:10.1016/j.physletb.2018.08.064. URL <http://dx.doi.org/10.1016/j.physletb.2018.08.064> 924  
 925  
 926  
 927  
 928  
 929  
 930  
 931  
 932  
 933  
 934  
 935  
 936  
 937  
 [21] A. P. Read, B. J. Chapman, C. U. Lei, J. C. Curtis, S. Ganjam, L. Kravitzman, L. Frunzio, R. J. Schoelkopf, Precision measurement of the microwave dielectric loss of sapphire in the quantum regime with parts-per-billion sensitivity, Phys. Rev. Appl. 19 (2023) 034064. doi:10.1103/PhysRevApplied.19.034064. URL <https://link.aps.org/doi/10.1103/PhysRevApplied.19.034064> 938  
 939  
 940  
 941  
 942  
 943  
 944  
 945  
 [22] J. M. Martinis, Saving superconducting quantum processors from decay and correlated errors generated by gamma and cosmic rays, npj Quantum Information 7 (1) (2021) 90. doi:10.1038/s41534-021-00431-0. URL <https://doi.org/10.1038/s41534-021-00431-0> 932  
 933  
 934  
 935  
 936  
 937  
 [23] A. Bargerbos, L. J. Splitthoff, M. Pita-Vidal, J. J. Wesdorp, Y. Liu, P. Krogsrød, L. P. Kouwenhoven, C. K. Andersen, L. Grünhaupt, Mitigation of quasi-particle loss in superconducting qubits by phonon scattering, Phys. Rev. Appl. 19 (2023) 024014. doi:10.1103/PhysRevApplied.19.024014. URL <https://link.aps.org/doi/10.1103/PhysRevApplied.19.024014> 941  
 942  
 943  
 944  
 945  
 [24] M. McEwen, et al., Resisting high-energy impact events through gap engineering in superconducting qubit arrays (2024). [arXiv:2402.15644](https://arxiv.org/abs/2402.15644). 946  
 947  
 [25] V. Iaia, et al., Phonon downconversion to suppress correlated errors in superconducting qubits, Nat Commun. 13 (6425) (2022). doi:<https://doi.org/10.1038/s41467-022-33997-0>. 949  
 950  
 951  
 952  
 [26] M. Kelsey, et al., G4cmp: Condensed matter physics simulation using the geant4 toolkit, Nuclear Instruments and Methods in Physics Research Section A: Accelerators, Spectrometers, Detectors and Associated Equipment 1055 (2023) 168473. doi:10.1016/j.nima.2023.168473. URL <http://dx.doi.org/10.1016/j.nima.2023.168473> 953  
 954  
 955  
 956  
 957  
 958  
 [27] S. Barman, G. P. Srivastava, Long-wavelength nonequilibrium optical phonon dynamics in cubic and hexagonal semiconductors, Phys. Rev. B 69 (2004) 235208. doi:10.1103/PhysRevB.69.235208. URL <https://link.aps.org/doi/10.1103/PhysRevB.69.235208> 961  
 962  
 963  
 964  
 965  
 966  
 [28] T. F. Harrelson, I. Hajar, O. A. Ashour, S. M. Griffin, Theoretical investigation of decoherence channels in 967  
 968

- 969 athermal phonon sensors (2023). [arXiv:2109.10988](https://arxiv.org/abs/2109.10988).  
970 [29] G. Srivastava, *The Physics of Phonons*, Taylor &  
971 Francis, 1990.  
972 URL <https://books.google.com/books?id=OE-bHd2gzVgC>  
973 [30] M. T. Labrot, A. P. Mayer, R. K. Wehner, P. E. Ober-  
974 mayer, Decay cascades of acoustic phonons in calcium  
975 fluoride, *Journal of Physics: Condensed Matter* 1 (45)  
976 (1989) 8809. [doi:10.1088/0953-8984/1/45/006](https://doi.org/10.1088/0953-8984/1/45/006).  
977 URL <https://dx.doi.org/10.1088/0953-8984/1/45/006>  
978 [31] A. Berke, A. Mayer, R. Wehner, Spontaneous decay of  
979 acoustic phonons in calcium fluoride and silicon, *Solid  
980 State Communications* 54 (5) (1985) 395–397. [doi:  
981 https://doi.org/10.1016/0038-1098\(85\)90933-0](https://doi.org/10.1016/0038-1098(85)90933-0).  
982 URL <https://www.sciencedirect.com/science/article/pii/0038109885909330>  
983 [32] A. Berke, A. P. Mayer, R. K. Wehner, Spontaneous  
984 decay of long-wavelength acoustic phonons, *Journal  
985 of Physics C: Solid State Physics* 21 (12) (1988) 2305.  
986 [doi:10.1088/0022-3719/21/12/014](https://doi.org/10.1088/0022-3719/21/12/014).  
987 URL <https://dx.doi.org/10.1088/0022-3719/21/12/014>  
988 [33] S.-i. Tamura, Spontaneous decay rates of la phonons  
989 in quasi-isotropic solids, *Phys. Rev. B* 31 (1985) 2574–  
990 2577. [doi:10.1103/PhysRevB.31.2574](https://doi.org/10.1103/PhysRevB.31.2574).  
991 URL <https://link.aps.org/doi/10.1103/PhysRevB.31.2574>  
992 [34] F. I. Fedorov, *General Theory of Elastic Waves in  
993 Crystals Based on Comparison with an Isotropic  
994 Medium*, Springer US, Boston, MA, 1968, pp. 169–  
995 209. [doi:10.1007/978-1-4757-1275-9\\_5](https://doi.org/10.1007/978-1-4757-1275-9_5).  
996 URL [https://doi.org/10.1007/978-1-4757-1275-9\\_5](https://doi.org/10.1007/978-1-4757-1275-9_5)  
997 [35] R. F. S. Hearmon, ‘Third-order’ elastic coefficients,  
998 *Acta Crystallographica* 6 (4) (1953) 331–340. [doi:  
999 https://doi.org/10.1107/S0365110X53000909](https://doi.org/10.1107/S0365110X53000909).  
1000 URL <https://doi.org/10.1107/S0365110X53000909>  
1001 [36] B. Campbell-Deem, P. Cox, S. Knapen, T. Lin,  
1002 T. Melia, Multiphonon excitations from dark matter  
1003 scattering in crystals, *Physical Review D* 101 (3)  
1004 (Feb. 2020). [doi:10.1103/physrevd.101.036006](https://doi.org/10.1103/physrevd.101.036006).  
1005 URL <https://dx.doi.org/10.1103/PhysRevD.101.036006>  
1006 [37] Y. Itin, F. W. Hehl, The constitutive tensor of linear  
1007 elasticity: Its decompositions, cauchy relations, null  
1008 lagrangians, and wave propagation, *Journal of Math-  
1009 ematical Physics* 54 (4) (Apr. 2013). [doi:10.1063/1.4801859](https://doi.org/10.1063/1.4801859).  
1010 URL [http://dx.doi.org/10.1063/1.4801859](https://dx.doi.org/10.1063/1.4801859)  
1011 [38] S.-i. Tamura, Isotope scattering of dispersive phonons  
1012 in ge, *Phys. Rev. B* 27 (1983) 858–866. [doi:10.1103/  
1013 PhysRevB.27.858](https://doi.org/10.1103/PhysRevB.27.858).  
1014 URL <https://link.aps.org/doi/10.1103/PhysRevB.27.858>  
1015 [39] S.-i. Tamura, Isotope scattering of large-wave-vector  
1016 phonons in gaas and insb: Deformation-dipole and  
1017 overlap-shell models, *Phys. Rev. B* 30 (1984) 849–854.  
1018 [doi:10.1103/PhysRevB.30.849](https://doi.org/10.1103/PhysRevB.30.849).  
1019 URL <https://link.aps.org/doi/10.1103/PhysRevB.30.849>  
1020 [40] R. Gurunathan, R. Hanus, G. Snyder, Alloy scatter-  
1021 ing of phonons, *Materials Horizons* 7 (6) (2020) 1452–  
1022 1456, publisher Copyright: © 2020 The Royal Society  
1023 of Chemistry. [doi:10.1039/c9mh01990a](https://doi.org/10.1039/c9mh01990a).  
1024 [41] D. T. Morelli, J. P. Heremans, G. A. Slack, Estimation  
1025 of the isotope effect on the lattice thermal conductivity  
1026 of group iv and group iii-v semiconductors, *Phys.  
1027 Rev. B* 66 (2002) 195304. [doi:10.1103/PhysRevB.66.  
1028 195304](https://doi.org/10.1103/PhysRevB.66.195304).  
1029 URL <https://link.aps.org/doi/10.1103/PhysRevB.66.195304>  
1030 [42] R. Hanus, R. Gurunathan, L. Lindsay, M. T. Agne,  
1031  
1032  
1033  
1034  
1035  
1036  
1037  
1038  
1039  
1040  
1041
- J. Shi, S. Graham, G. Jeffrey Snyder, Thermal transport in defective and disordered materials, *Applied Physics Reviews* 8 (3) (2021) 031311. [arXiv:https://doi.org/10.1063/5.0055593](https://doi.org/10.1063/5.0055593)  
1042 URL <https://doi.org/10.1063/5.0055593>  
1043 [43] N. H. Protik, C. Draxl, Beyond the tamura model of  
1044 phonon-isotope scattering, *Phys. Rev. B* 109 (2024)  
1045 165201. [doi:10.1103/PhysRevB.109.165201](https://doi.org/10.1103/PhysRevB.109.165201).  
1046 URL <https://link.aps.org/doi/10.1103/PhysRevB.109.165201>  
1047 [44] A. Jain, S. P. Ong, G. Hautier, W. Chen, W. D.  
1048 Richards, S. Dacek, S. Cholia, D. Gunter, D. Skinner,  
1049 G. Ceder, K. A. Persson, Commentary: The Materials Project: A materials genome approach to accelerating materials innovation, *APL Materials* 1 (1) (2013) 011002. [arXiv:https://doi.org/10.1063/1.4812323](https://doi.org/10.1063/1.4812323)  
1050 URL <https://doi.org/10.1063/1.4812323>  
1051 [45] A. Togo, L. Chaput, T. Tadano, I. Tanaka, Implementation strategies in phonopy and phono3py, *J. Phys. Condens. Matter* 35 (35) (2023) 353001. [doi:10.1088/1361-648X/acd831](https://doi.org/10.1088/1361-648X/acd831).  
1052 URL <https://doi.org/10.1088/1361-648X/acd831>  
1053 [46] A. Togo, First-principles phonon calculations with phonopy and phono3py, *J. Phys. Soc. Jpn.* 92 (1) (2023) 012001. [doi:10.7566/JPSJ.92.012001](https://doi.org/10.7566/JPSJ.92.012001).  
1054 URL <https://doi.org/10.7566/JPSJ.92.012001>  
1055 [47] S. M. Griffin, K. Inzani, T. Trickle, Z. Zhang, K. M. Zurek, Multichannel direct detection of light dark matter: Target comparison, *Phys. Rev. D* 101 (5) (2020) 055004. [arXiv:1910.10716](https://arxiv.org/abs/1910.10716), [doi:10.1103/PhysRevD.101.055004](https://doi.org/10.1103/PhysRevD.101.055004).  
1056 URL <https://doi.org/10.1103/PhysRevD.101.055004>  
1057 [48] F. Rösch, O. Weis, Geometric propagation of acoustic phonons in monocrystals within anisotropic continuum acoustics, *Zeitschrift für Physik B Condensed Matter* 25 (2) (1976) 101–114. [doi:10.1007/BF01320167](https://doi.org/10.1007/BF01320167).  
1058 URL <https://doi.org/10.1007/BF01320167>  
1059 [49] S. Leman, Review article: Physics and monte carlo techniques as relevant to cryogenic, phonon and ionization readout of cdms radiation-detectors (09 2011).  
1060 URL <https://doi.org/10.1088/0959-6273/20/9/095001>  
1061 [50] G. A. Northrop, J. P. Wolfe, Ballistic phonon imaging in solids—a new look at phonon focusing, *Phys. Rev. Lett.* 43 (1979) 1424–1427. [doi:10.1103/PhysRevLett.43.1424](https://doi.org/10.1103/PhysRevLett.43.1424).  
1062 URL <https://doi.org/10.1103/PhysRevLett.43.1424>  
1063 [51] J. P. Wolfe, Imaging Phonons: Acoustic Wave Propagation in Solids, Cambridge University Press, 1998.  
1064 URL <https://doi.org/10.1017/CBO9780511541264>  
1065 [52] K. Jakata, A. Every, Frequency dependence of dispersive phonon images : research article, *South African Journal of Science* 104 (9) (2008) 374–378. [arXiv:https://journals.co.za/doi/pdf/10.10520/EJC96837](https://doi.org/10.1080/00382710.2008.11436273), [doi:10.10520/EJC96837](https://doi.org/10.10520/EJC96837).  
1066 URL <https://doi.org/10.10520/EJC96837>  
1067 [53] A. G. Every, G. L. Koos, J. P. Wolfe, Ballistic phonon imaging in sapphire: Bulk focusing and critical-cone channeling effects, *Phys. Rev. B* 29 (1984) 2190–2209. [doi:10.1103/PhysRevB.29.2190](https://doi.org/10.1103/PhysRevB.29.2190).  
1068 URL <https://doi.org/10.1103/PhysRevB.29.2190>  
1069 [54] S.-i. Tamura, T. Harada, Focusing of large-wave-vector phonons in gaas, *Phys. Rev. B* 32 (1985) 5245–5250. [doi:10.1103/PhysRevB.32.5245](https://doi.org/10.1103/PhysRevB.32.5245).  
1070 URL <https://doi.org/10.1103/PhysRevB.32.5245>  
1071 [55] M. Msall, T. Head, D. Jumper, Low-temperature group velocity and elasticity in cawo4, *Solid State Communications* 150 (27) (2010) 1192–1195. [doi:https://doi.org/10.1016/j.ssc.2010.04.014](https://doi.org/10.1016/j.ssc.2010.04.014).  
1072 URL <https://doi.org/10.1016/j.ssc.2010.04.014>

- article/pii/S0038109810002292
- [56] C. V. Briscoe, C. F. Squire, Elastic constants of lif from 4.2°K to 300°K by ultrasonic methods, Phys. Rev. 106 (1957) 1175–1177. doi:10.1103/PhysRev.106.1175.  
URL <https://link.aps.org/doi/10.1103/PhysRev.106.1175>
- [57] H. J. Maris, S. Tamura, Propagation of acoustic phonon solitons in nonmetallic crystals, Phys. Rev. B 84 (2011) 024301. doi:10.1103/PhysRevB.84.024301.  
URL <https://link.aps.org/doi/10.1103/PhysRevB.84.024301>
- [58] R. Baumgartner, M. Engelhardt, K. F. Renk, Spontaneous decay of high-frequency acoustic phonons in  $\text{CaF}_2$ , Phys. Rev. Lett. 47 (1981) 1403–1407. doi:10.1103/PhysRevLett.47.1403.  
URL <https://link.aps.org/doi/10.1103/PhysRevLett.47.1403>
- [59] J. Wigmore, A. Kozorezov, H. bin Rani, M. Giltrow, H. Kraus, B. Taele, Scattering of thz phonons, Physica B: Condensed Matter 316–317 (2002) 589–591, proceedings of the 10th International Conference on Phonon Scattering in Condensed Matter. doi:[https://doi.org/10.1016/S0921-4526\(02\)00581-1](https://doi.org/10.1016/S0921-4526(02)00581-1).  
URL <https://www.sciencedirect.com/science/article/pii/S0921452602005811>
- [60] K. Hayasaka, R. Higashi, J. Suda, Y. Tanaka, S. Tamura, M. Giltrow, J. Wigmore, Anomalous mode, elastic constants and phonon images in cawo4, Solid State Communications 143 (8) (2007) 386–389. doi:<https://doi.org/10.1016/j.ssc.2007.06.018>.  
URL <https://www.sciencedirect.com/science/article/pii/S0038109807004589>
- [61] S. Tamura, J. Shields, M. Ramsbey, J. Wolfe, Measurements of phonon elastic scattering rates by phonon imaging and monte-carlo simulation, in: Phonon Scattering in Condensed Matter VII: Proceedings of the Seventh International Conference, Cornell University, Ithaca, New York, August 3–7, 1992, Springer, 1993, pp. 79–83.
- [62] J. A. Harrington, C. T. Walker, Phonon Scattering by Point Defects in  $\text{CaF}_2$ ,  $\text{SrF}_2$ , and  $\text{BaF}_2$ , Phys. Rev. B 1 (1970) 882–890. doi:10.1103/PhysRevB.1.882.  
URL <https://link.aps.org/doi/10.1103/PhysRevB.1.882>
- [63] J. R. de Laeter, J. K. Böhlke, P. D. Bièvre, H. Hidaka, H. S. Peiser, K. J. R. Rosman, P. D. P. Taylor, Atomic weights of the elements. review 2000 (iu-pac technical report), Pure and Applied Chemistry 75 (6) (2003) 683–800 [cited 2024-06-05]. doi:doi:10.1351/pac200375060683.  
URL <https://doi.org/10.1351/pac200375060683>
- [64] I. Richman, Longitudinal Optical Phonons in  $\text{CaF}_2$ ,  $\text{SrF}_2$ , and  $\text{BaF}_2$ , The Journal of Chemical Physics 41 (9) (1964) 2836–2837. arXiv: [https://pubs.aip.org/aip/jcp/article-pdf/41/9/2836/18836140/2836\\_1\\_online.pdf](https://pubs.aip.org/aip/jcp/article-pdf/41/9/2836/18836140/2836_1_online.pdf), doi:10.1063/1.1726360.  
URL <https://doi.org/10.1063/1.1726360>
- [65] D. von der Linde, J. Kuhl, H. Klingenberg, Raman scattering from nonequilibrium lo phonons with picosecond resolution, Phys. Rev. Lett. 44 (1980) 1505–1508. doi:10.1103/PhysRevLett.44.1505.  
URL <https://link.aps.org/doi/10.1103/PhysRevLett.44.1505>
- [66] J. Shan, F. Wang, E. Knoesel, M. Bonn, T. F. Heinz, Measurement of the frequency-dependent conductivity in sapphire, Phys. Rev. Lett. 90 (2003) 247401. doi:10.1103/PhysRevLett.90.247401.  
URL <https://link.aps.org/doi/10.1103/PhysRevLett.90.247401>
- [67] H. J. Hou, H. Guan, S. R. Zhang, L. H. Xie, L. Wang, Structural, phonon and thermodynamic properties of the rocksalt structure lif from first principles, in: Methods of Design and Characterization of Materials, Research and Development of Technological Processes, Vol. 850 of Materials Science Forum, Trans Tech Publications Ltd, 2016, pp. 348–353. doi:10.4028/www.scientific.net/MSF.850.348.  
[68] I. Richman, Longitudinal Optical Phonons in  $\text{CaF}_2$ ,  $\text{SrF}_2$ , and  $\text{BaF}_2$ , The Journal of Chemical Physics 41 (9) (1964) 2836–2837. arXiv: [https://pubs.aip.org/aip/jcp/article-pdf/41/9/2836/18836140/2836\\_1\\_online.pdf](https://pubs.aip.org/aip/jcp/article-pdf/41/9/2836/18836140/2836_1_online.pdf), doi:10.1063/1.1726360.  
URL <https://doi.org/10.1063/1.1726360>
- [69] J. Suda, T. Sato, Temperature dependence of the linewidth of the first-order raman spectra for cawo 4 crystal, Journal of the Physical Society of Japan 66 (6) (1997) 1707–1713. arXiv: <https://doi.org/10.1143/JPSJ.66.1707>. doi:10.1143/JPSJ.66.1707.  
URL <https://doi.org/10.1143/JPSJ.66.1707>
- [70] A. G. Every, G. L. Koos, J. P. Wolfe, Ballistic phonon imaging in sapphire: Bulk focusing and critical-cone channeling effects, Phys. Rev. B 29 (1984) 2190–2209. doi:10.1103/PhysRevB.29.2190.  
URL <https://link.aps.org/doi/10.1103/PhysRevB.29.2190>
- [71] G. A. Northrop, S. E. Hebboul, J. P. Wolfe, Lattice dynamics from phonon imaging, Phys. Rev. Lett. 55 (1985) 95–98. doi:10.1103/PhysRevLett.55.95.  
URL <https://link.aps.org/doi/10.1103/PhysRevLett.55.95>
- [72] G. A. Northrop, E. J. Cotts, A. C. Anderson, J. P. Wolfe, Phonon imaging of highly dislocated lif, Phys. Rev. Lett. 49 (1982) 54–57. doi:10.1103/PhysRevLett.49.54.  
URL <https://link.aps.org/doi/10.1103/PhysRevLett.49.54>
- [73] D. C. Hurley, J. P. Wolfe, Phonon focusing in cubic crystals, Phys. Rev. B 32 (1985) 2568–2587. doi:10.1103/PhysRevB.32.2568.  
URL <https://link.aps.org/doi/10.1103/PhysRevB.32.2568>
- [74] S. M. Griffin, Y. Hochberg, K. Inzani, N. Kurinsky, T. Lin, T. C. Yu, Silicon carbide detectors for sub-gev dark matter, Phys. Rev. D 103 (2021) 075002. doi:10.1103/PhysRevD.103.075002.  
URL <https://link.aps.org/doi/10.1103/PhysRevD.103.075002>
- [75] S. Watkins, Searching for Light Dark Matter with Narrow-Gap Semiconductors: The SPLENDOR Experiment, tAUP 2023 (2023).
- [76] A. Agrawal, et al., Development of MMC-based lithium molybdate cryogenic calorimeters for AMoRE-II (2024). arXiv: [2407.12227](https://arxiv.org/abs/2407.12227). URL <https://arxiv.org/abs/2407.12227>
- [77] V. Dompè, et al., Expected sensitivity to 128Te neutrinoless double beta decay with the CUORE TeO<sub>2</sub> cryogenic bolometers, J Low Temp Phys. 209 (2022) 788–795. doi: <https://doi.org/10.1007/s10909-022-02738-4>.
- [78] R. C. Tripathi, G. S. Verma, Third-Order Elastic Constants of Ge at Room and Liquid-Nitrogen Temperatures, Journal of Applied Physics 41 (7) (1970) 2999–3002. arXiv: [https://pubs.aip.org/aip/jap/article-pdf/41/7/2999/18354708/2999\\_1\\_online.pdf](https://pubs.aip.org/aip/jap/article-pdf/41/7/2999/18354708/2999_1_online.pdf), doi:10.1063/1.1659352.  
URL <https://doi.org/10.1063/1.1659352>
- [79] M. T. Labrot, A. P. Mayer, R. K. Wehner, P. E. Obermayer, Decay cascades of acoustic phonons in calcium fluoride, Journal of Physics: Condensed Matter 1 (45) (1989) 8809. doi:10.1088/0953-8984/1/45/006.  
URL <https://dx.doi.org/10.1088/0953-8984/1/45/006>
- [80] S. Mori, Y. Hiki, Calculation of the third- and fourth-

- 1261 order elastic constants of alkali halide crystals, Journal  
1262 of the Physical Society of Japan 45 (5) (1978)  
1263 1449–1456. [arXiv:https://doi.org/10.1143/JPSJ.45.1449](https://doi.org/10.1143/JPSJ.45.1449).  
1264 [45.1449](https://doi.org/10.1143/JPSJ.45.1449), doi:10.1143/JPSJ.45.1449.  
1265 URL <https://doi.org/10.1143/JPSJ.45.1449>
- 1266 [81] R. E. Hankey, D. E. Schuele, **Third-Order Elastic  
1267 Constants of Al<sub>2</sub>O<sub>3</sub>**, The Journal of the Acoustical  
1268 Society of America 48 (1B) (2005) 190–202. [arXiv:  
1269 https://pubs.aip.org/asa/jasa/article-pdf/48/1B/190/11610699/190\\\_\\\_1\\_online.pdf](https://pubs.aip.org/asa/jasa/article-pdf/48/1B/190/11610699/190\_\_1_online.pdf),  
1270 doi:10.1121/1.1912116.  
1271 URL <https://doi.org/10.1121/1.1912116>
- 1272 [82] P. Blanchfield, A. Miller, G. Saunders, **Acoustic  
1273 symmetry and the third order elastic constants of  
1274 tetragonal tii (4/m) crystals**, Journal of Physics and  
1275 Chemistry of Solids 44 (6) (1983) 569–577. doi:  
1276 [https://doi.org/10.1016/0022-3697\(83\)90047-1](https://doi.org/10.1016/0022-3697(83)90047-1).  
1277 URL [https://www.sciencedirect.com/science/  
1278 article/pii/0022369783900471](https://www.sciencedirect.com/science/article/pii/0022369783900471)
- 1279